

Visible light wavefront sensorless adaptive optics optical coherence tomography

**by
Christine Huang**

BASc (Hons., Engineering Science), Simon Fraser University, 2016

Thesis Submitted in Partial Fulfillment of the
Requirements for the Degree of
Master of Applied Science

in the
School of Engineering Science
Faculty of Applied Science

© Christine Huang 2018
SIMON FRASER UNIVERSITY
Spring 2018

Copyright in this work rests with the author. Please ensure that any reproduction or re-use is done in accordance with the relevant national copyright legislation.

Approval

Name: **Christine Huang**

Degree: **Master of Applied Science**

Title: **Visible light wavefront sensorless adaptive optics
optical coherence tomography**

Examining Committee: **Chair: Pierre Lane**
Associate Professor of Professional Practice

Marinko Sarunic
Senior Supervisor
Professor
School of Engineering Science

Mirza Faisal Beg
Internal Examiner
Professor
School of Engineering Science

Yifan Jian
Technical Supervisor
Research Professor
School of Engineering Science

Date Defended/Approved: January 11, 2018

Ethics Statement

The author, whose name appears on the title page of this work, has obtained, for the research described in this work, either:

- a. human research ethics approval from the Simon Fraser University Office of Research Ethics

or

- b. advance approval of the animal care protocol from the University Animal Care Committee of Simon Fraser University

or has conducted the research

- c. as a co-investigator, collaborator, or research assistant in a research project approved in advance.

A copy of the approval letter has been filed with the Theses Office of the University Library at the time of submission of this thesis or project.

The original application for approval and letter of approval are filed with the relevant offices. Inquiries may be directed to those authorities.

Simon Fraser University Library
Burnaby, British Columbia, Canada

Update Spring 2016

Abstract

Advancements in optical imaging technology have revolutionized clinical ophthalmology. Optical Coherence Tomography (OCT) is routinely used for cross-sectional human retinal imaging and diagnosis of vision robbing diseases. Although most OCT imaging has been performed using light in the near infrared, visible light (VIS) has also been recently used. Retinal VIS-OCT has been reported in both small animals, and in humans. While OCT cross-sectional images of the retina allow for detailed visualization of the retinal structure and analysis of pathology, fluorescence imaging is capable of visualizing the biological function of the retina through labeled reporter cells. Using a single supercontinuum broadband visible light source, VIS-OCT and confocal Scanning Laser Ophthalmoscopy (SLO) are combined as a multi-modal system for simultaneous structural and functional imaging of the mouse retina. The large numerical aperture of the mouse eye permits imaging at sub-micrometer resolution. However, aberrations are introduced from the tear film, cornea, and intraocular lens, making adaptive optics (AO) a vital methodology to improve the lateral resolution in small animal eye imaging. Depth-resolved, sensorless adaptive optics (SAO) for single photon fluorescence excitation is presented, and has been adapted to small animal retinal imaging applications. The coherence-gated, depth resolved VIS-OCT images are used for image-guided SAO aberration correction when the fluorescent signal is too weak, providing perfectly registered structural and functional images of the mouse retina in high resolution.

Acknowledgements

This thesis has benefited from the support of many people, some of whom I would like to sincerely thank.

Firstly, I would like to express my gratitude to my supervisor, Dr. Marinko V. Sarunic, for allowing me the opportunity to work as a member in the Biomedical Optics Research Group (BORG). He has provided me with his expertise, patience, and guidance throughout the progress of my thesis.

I would also like to thank the rest of my thesis committee, Dr. Mirza Faisal Beg and Dr. Yifan Jian for their continued guidance and support in this research.

I am very grateful to be part of the BORG. I am especially grateful to BORG member, Dr. Myeonjin Ju, for his mentorship, time, and many contributions to the thesis. I would like to thank Mr. Daniel Wahl, for all his time, patience, and mentorship he provided me throughout this learning process. Finally, I would like to acknowledge and thank Mr. Ryne Watterson for his design of the spectrometer. To the rest of the BORG team, thank you for sharing your support and encouragement.

Lastly, I would like to thank my family and friends for their continued love and encouragement in all my endeavours.

Table of Contents

Approval.....	ii
Ethics Statement.....	iii
Abstract.....	iv
Acknowledgements.....	v
Table of Contents.....	vi
List of Tables.....	viii
List of Figures.....	ix
List of Symbols.....	xi
List of Acronyms.....	xii
Chapter 1. Introduction.....	1
1.1. Visible Light Optical Coherence Tomography.....	1
1.2. Mouse Retinal Imaging.....	2
1.3. Adaptive Optics.....	3
1.4. WSAO VIS-OCT and Fluorescence Imaging.....	5
1.5. Thesis Organization.....	6
Chapter 2. Adaptive Optics in Ophthalmic Imaging.....	7
2.1. Overview of Adaptive Optics.....	7
2.2. Wavefront Corrector.....	8
2.3. Wavefront Sensor.....	9
2.4. Polarization Optics.....	11
2.5. Wavefront Sensorless Adaptive Optics.....	11
2.5.1. Image Optimization.....	11
2.5.2. Zernike Polynomials.....	12
2.6. Depth Resolved Image-Guided WSAO.....	14
2.7. Summary.....	15
Chapter 3. Methods.....	16
3.1. System Characterization.....	16
3.1.1. Axial Resolution.....	16
3.1.2. Sensitivity.....	17
3.2. System Design.....	19
3.2.1. System Topology.....	19
3.2.2. Longitudinal Chromatic Aberrations.....	23
3.2.3. Spectrometer Design and Calibration.....	24
3.3. Summary.....	25
Chapter 4.	27
4.1. Mouse Handling.....	27
4.2. Adaptive Optics Image Acquisition Parameters.....	27
4.2.1. Image Acquisition.....	27

4.2.2. Image Processing	28
4.3. Results	29
4.3.1. Phantom Imaging	29
4.3.2. VIS-OCT Low Numerical Aperture Imaging	30
4.3.3. <i>In-vivo</i> AO VIS-OCT and Fluorescence Imaging	31
4.4. Discussion	34
Chapter 5. Future Work.....	35
5.1. VIS-OCT for Retinal Oximetry.....	35
5.2. VIS-OCT WSAO by Pupil Segmentation.....	36
5.3. VIS-OCT with Multi-Fluorescence Imaging	37
References.....	41

List of Tables

Table 1: Summary of Zernike polynomials up to the 4th radial order	13
Table 2: Summary of theoretical and measured axial resolution.....	17
Table 3: Summary of theoretical and measured SNR.....	19

List of Figures

Figure 1: Example schematic of a multi-modal spectral domain VIS-OCT and cSLO imaging system. A dichroic mirror (DC) is used to separate the fluorescence from the back-scattered light from the sample.	2
Figure 2: Comparison of the human and mouse eye. The mouse eye has a larger numerical aperture, and a shorter focal length making the retina appear optically thick. The mouse eye has been scaled to the human size for comparison.	3
Figure 3: Schematic of a closed loop AO system using a SHWFS for wavefront measurement and a deformable mirror to correct aberrations.	4
Figure 4: (a) Diffraction limited focus spot is achieved when there are no aberrations in a system or sample. (b) Focal spot is degraded due to aberrations in the sample.	8
Figure 5: Segmented deformable mirror from IrisAO. [Credit: IrisAO, Inc.]	9
Figure 6: (a) A planar wavefront incident on the lenslet array produces a perfect lattice of point images. (b) An aberrated wavefront causes the focal spots to shift across the camera.....	10
Figure 7: Flow chart of the hill-climbing modal search algorithm.....	12
Figure 8: Zernike polynomials ordered vertically by radial degree.	14
Figure 9: Schematic of a common path interferometer used to measure the axial resolution. Light is emitted from the source, split into two arms by a 50/50 beam splitter, then recombined at the spectrometer.....	17
Figure 10: System used to calculate SNR and sensitivity roll-off. A mirror is placed at the end of each arm. The reference arm is translated by a distance of Δz , with a dispersion compensation block (DCB) to match the sample arm. A neutral density (ND) filter is placed in the sample arm to avoid saturation on the line scan camera (LSC).....	18
Figure 11: Sensitivity roll-off curve.....	19
Figure 12: Multimodal VIS-OCT and fluorescence imaging system. Light emitted from the supercontinuum source is coupled into a single mode 50/50 fiber coupler with a polarization controller (PC) in the reference and sample arm. Light passes through a dichroic mirror (DC), then to the DM. $\{L_1, L_2, L_3, L_4\} = \{200\text{m}, 200\text{mm}, 150\text{mm}, 100\text{mm}\}$. Light is scanned over the retina with the galvanometer mirrors (GM). $\{L_5, L_6\} = \{100\text{mm}, 30\text{mm}\}$. The reference arm is implemented in a cat's-eye configuration, with a dispersion compensation block (DCB). Back scattered light is detected with the spectrometer, consisting of a diffraction grating (DG) and line scan camera (LSC). Fluorescence is detected with the confocal detection channel, using a photomultiplier tube (PMT) as the detector.	21
Figure 13: Image of the multimodal VIS-OCT and fluorescence imaging system.....	22
Figure 14: (a) Source spectrum using only achromatic lenses in the system. (b) Aspheric lenses cause chromatic aberrations, resulting in narrowing of the source spectrum.	23

Figure 15: Spectrometer used in the detection channel of the VIS-OCT system. $\{f_{\text{collimator}}, f_{\text{focusing}}\} = \{60\text{mm}, 200\text{mm}\}$	25
Figure 16: (a),(b) <i>En-face</i> OCT and fluorescence images before aberration correction and (c),(d) after correction. (e) Line spread function taken across the dashed lines demonstrating the performance of the correction.....	29
Figure 17: Left: Single frame B-scan. Right: An average of 100 B-scans.....	30
Figure 18: Left: Single frame B-scan. Right: An average of 200 B-scans.....	30
Figure 19: (a) B-scan (b) <i>En-face</i> image of the NFL. Each image is an average of 3 frames.	31
Figure 20: (a),(b) OCT B-scan and fluorescein angiography before optimization and (c),(d) after aberration correction. Scale bar, 30 μm . (e) The Zernike coefficients selected during the optimization are demonstrated.....	32
Figure 21: (a),(b),(c) B-scan and EGFP labelled ganglion cell before optimization, and (d),(e),(f) the optimized images. Scale bar, 30 μm . (g) The line spread function taken across the arrows labelled in (c) and (f). (h) The Zernike coefficients selected during optimization are demonstrated.....	33
Figure 22: 6 μm fluorescent beads with aberration correction (AO on) and without (AO off). (a) and (b) are an average of 30 frames. Scale bar, 6 μm . (c) Wavefront aberration map. (d) Normalized intensity at the dashed lines indicating a ~30% increase. (e) Zernike coefficients for the corrected wavefront.	38
Figure 23: (a,b,e,f) PSAO for retinal fluorescein angiography with aberration correction (AO on) and without (AO off) for two mice. Scale bars, 20 μm . (c,g) Zernike coefficients for the corrected wavefront. (d) The normalized intensity at the location of the dashed lines had a ~30% increase in the peak intensity after correction. (h) The wavefront aberration map for the bottom panel.	39
Figure 24: SLO images acquired using polarization optics to remove specular reflections from lenses.	40
Figure 25: SLO and fluorescence imaging acquired at the same location using the same light source.....	40

List of Symbols

e	Electronic charge
I_j	Intensity value at j-th pixel
$J(\mathbf{k})$	Merit function
\mathbf{k}	Zernike coefficient vector
l_c	Coherence length
m	Zernike polynomial angular frequency
M_i	Modal coefficient
n	Zernike polynomial radial order
P_s	Power reflected from sample arm
r	Distance in polar coordinates
R	Radial polynomial
R_s	Reflectivity of sample arm
$w(\mathbf{k})$	Wavefront shape
$Z_i(r, \theta)$	Zernike polynomial
θ	Radial angle in polar coordinates
$\Psi(r, \theta)$	Aberration function
λ_0	Center wavelength
$\Delta\lambda$	Bandwidth
Δt	Camera exposure time
ρ	Detector responsivity

List of Acronyms

AO	Adaptive Optics
CCD	Charge-Coupled Device
CMOS	Complementary Metal Oxide Semiconductor
cSLO	Confocal Scanning Laser Ophthalmoscopy
DM	Deformable Mirror
DOF	Depth of Focus
EGFP	Enhanced Green Fluorescent Protein
EYFP	Enhanced Yellow Fluorescent Protein
FWHM	Full Width at Half Maximum
Hb	Deoxygenated Hemoglobin
HbO ₂	Oxygenated Hemoglobin
LCA	Longitudinal Chromatic Aberrations
LUT	Look Up Table
NA	Numerical Aperture
NIR	Near Infrared
NFL	Nerve Fiber Layer
OCT	Optical Coherence Tomography
OPL	Outer Plexiform Layer
PMT	Photomultiplier Tube
PSAO	Pupil Segmentation Adaptive Optics
PSF	Point Spread Function
SLO	Scanning Laser Ophthalmoscopy
sO ₂	Retinal Blood Oxygen Saturation Rate
SNR	Signal to Noise Ratio
SHWFS	Shack-Hartmann Wavefront Sensor
VIS	Visible Light
WSAO	Wavefront Sensorless Adaptive Optics

Chapter 1. Introduction

1.1. Visible Light Optical Coherence Tomography

Vision robbing diseases, such as age-related macular degeneration, and glaucoma, heavily affect the quality of life. Development of new therapies for these diseases is an active area of research [1]. Advancements in non-invasive, optical imaging technology have had a significant impact in clinical ophthalmology. In particular, optical coherence tomography (OCT) is routinely used for cross-sectional retinal imaging and diagnosis using near infrared (NIR) light. Multi-modal systems are commercially available that combine OCT with fundus photography or confocal scanning laser ophthalmoscopy (cSLO) using visible light to excite fluorescence in the retina. A few research groups have adapted these OCT and cSLO systems designed for human imaging to visualize the retina in small animal eyes, such as [2]–[4].

More recently, visible light OCT (VIS-OCT) [5] has been introduced to retinal imaging in both small animals [6]–[9], and humans [10]–[12]. The results are encouraging for high quality retinal imaging, and measurement of retinal blood oxygenation [8], [9], [13]–[15]. Visible light is strongly absorbed by potential retinal pathology biomarkers such as melanin, hemoglobin, and photopigment [16]. The strong absorption from hemoglobin enables quantitative measurement and mapping of this molecule with VIS-OCT. Additionally, compared to traditional NIR-OCT, VIS-OCT inherently has a higher lateral resolution at a given numerical aperture (NA), and a higher axial resolution at a given bandwidth (the axial resolution is inversely proportional to the square of the central wavelength). Using a single supercontinuum light source, VIS-OCT can be combined with fluorescence imaging to provide simultaneous acquisition of structural and functional images that are perfectly co-aligned with one another. Figure 1 demonstrates a spectral domain VIS-OCT system combined with a fluorescence cSLO channel using a single light source.

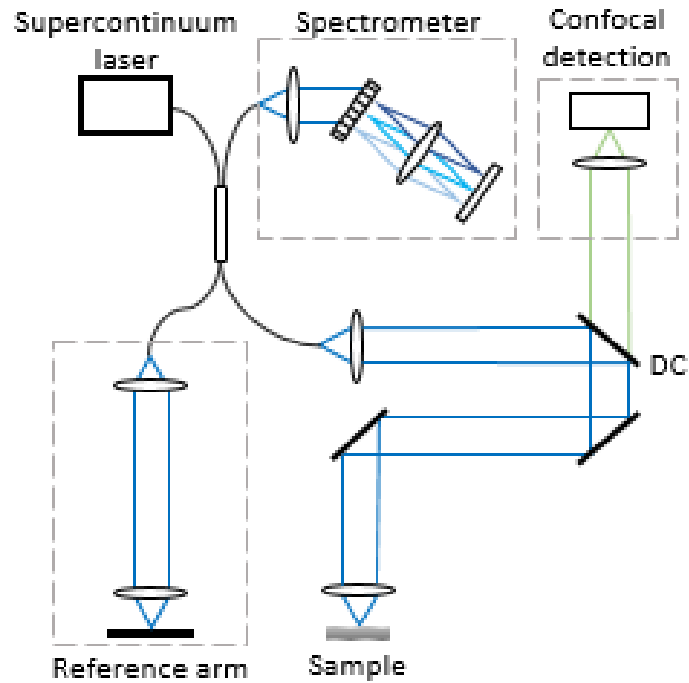


Figure 1: Example schematic of a multi-modal spectral domain VIS-OCT and cSLO imaging system. A dichroic mirror (DC) is used to separate the fluorescence from the back-scattered light from the sample.

1.2. Mouse Retinal Imaging

Vision research commonly uses small animal models of human vision-robbing diseases, particularly mice, because they are inexpensive, and versatile to genetic manipulations. Non-invasive optical imaging of the mouse retina permits diseases to be characterized and the effects of potential therapies to be studied *in vivo* and longitudinally. The mouse eye is well suited for high-resolution, non-invasive optical imaging due to its large NA. The maximum pupil diameter of a mouse eye is $\sim 2\text{mm}$, corresponding to an estimated numerical aperture of ~ 0.5 [17], and theoretically attainable sub-micrometer lateral resolution. In order to increase the NA, the diameter of the beam incident on the mouse cornea also needs to be increased. With a large NA, (ie. filling the pupil) aberrations are exacerbated from the tear film, cornea and intraocular lens, degrading the quality of the focused spot. Based on biometric measurements of the mouse eye, diffraction limited imaging is only achieved with a maximum collimated beam with diameter of $\sim 0.9\text{ mm}$ incident on the pupil [18].

Increasing the beam diameter beyond that increases wavefront distortion and thus lowers the actual resolution.

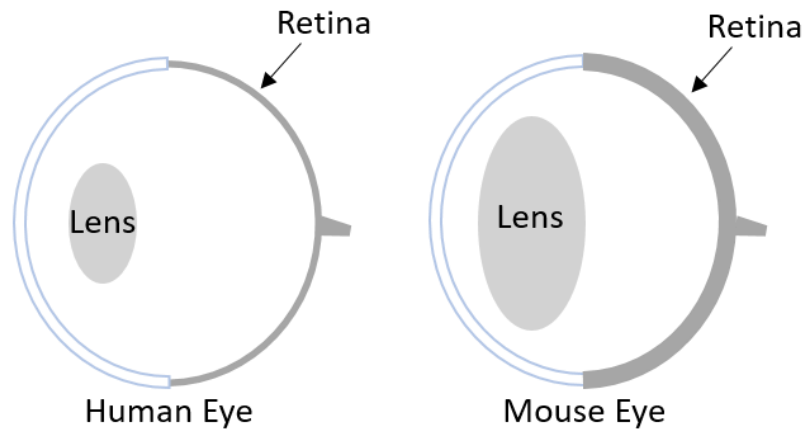


Figure 2: Comparison of the human and mouse eye. The mouse eye has a larger numerical aperture, and a shorter focal length making the retina appear optically thick. The mouse eye has been scaled to the human size for comparison.

1.3. Adaptive Optics

In order to approach diffraction limited *in-vivo* imaging with the maximum NA, the aberrations introduced by the eye can be compensated using adaptive optics (AO), a technique that was originally developed in the field of astronomy [19]. When applied to retinal imaging, the conventional approach to AO makes a measurement of the total ocular wavefront aberrations using a Shack-Hartmann wavefront sensor (SHWFS), and compensates the distorted wavefront in a closed feedback loop by shaping a deformable mirror (DM) [20], [21]. A schematic of a closed loop AO system is shown in Figure 3.

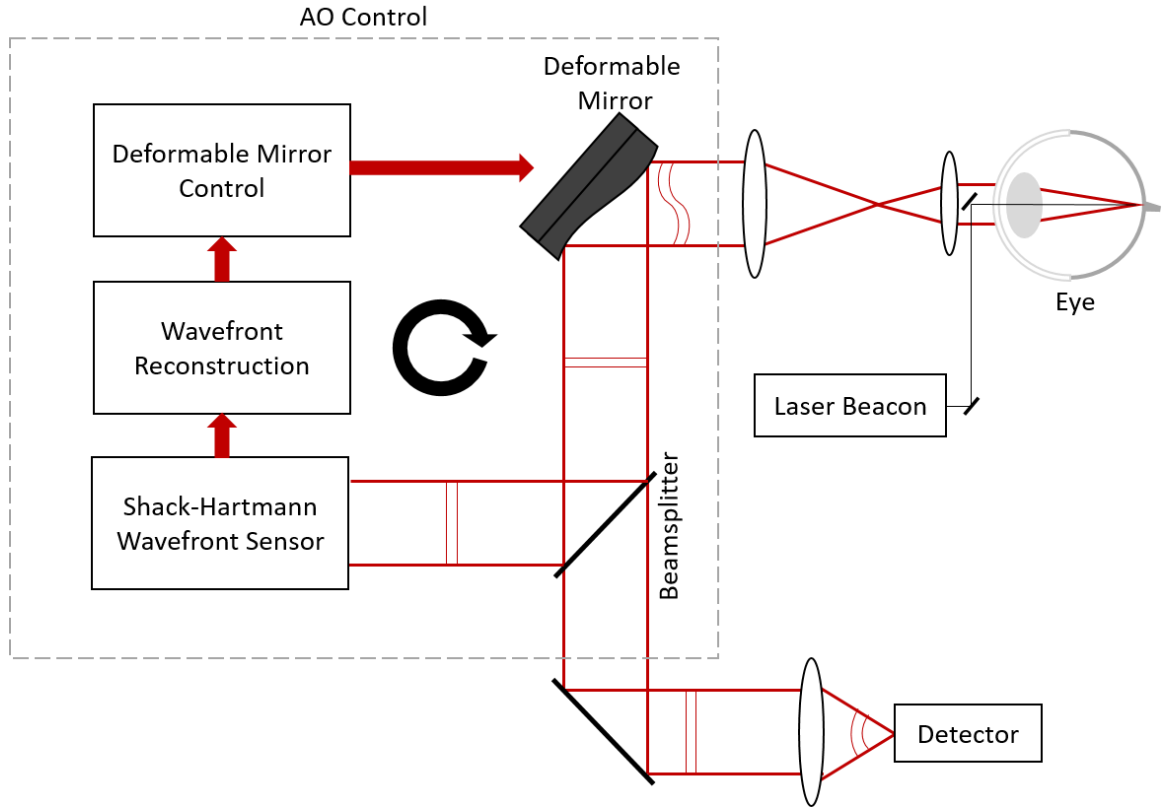


Figure 3: Schematic of a closed loop AO system using a SHWFS for wavefront measurement and a deformable mirror to correct aberrations.

Wavefront sensing in mice has been previously reported with excellent results [22]–[24]. The first examples of improved resolution for small animal retinal imaging was with AO cSLO based instruments. Biss *et al.* and Alt *et al.* demonstrated AO biomicroscope *in-vivo* imaging systems for the mouse retina, demonstrating that AO correction increases the brightness and lateral resolution in retinal images [25]–[27]. While this method has demonstrated excellent aberration correction ability for rodent imaging, SHWFS-based approaches can be challenging as they are sensitive to wavefront reconstruction errors produced by non-common path errors, multiple reflective retinal planes (the ‘small eye artifact’), and specular reflections [28].

In order to resolve the limitations associated with the SHWFS and to extend the applications of AO imaging systems, wavefront sensorless adaptive optics (WSAO) systems have been developed [29], [30]. Wavefront sensorless AO is an alternative method that uses images acquired with the optical system to determine the optimal shape of a deformable element to correct the wavefront aberrations. WSAO has

demonstrated promising results in microscopy, as well as retinal imaging in humans and mice [26], [31]–[33]. A method that is common to many WSAO reports is iteratively changing the shape of the DM while optimizing an image quality metric [30]. Alternative methods include pupil segmentation adaptive optics [34], which indirectly measures a wavefront using images acquired with different regions of the imaging pupil to determine the gradient of the wavefront at each pupil location.

1.4. WSAO VIS-OCT and Fluorescence Imaging

AO for human retinal imaging has been integrated with cSLO [35]–[37], OCT [38], [39], as well as with flood illumination fundus photography [40]. In addition to improving the lateral resolution, high NA imaging is also associated with short depth of focus, which is particularly important for depth resolved confocal detection of fluorescence excited in the retina. The fluorescence images acquired with conventional cSLO are two dimensional, and do not have adequate axial resolution to determine in which retinal layer the fluorescent molecules are located. AO SLO provides optical sectioning, but does not provide direct information as to where in the retina the focus is located. Furthermore, depending on the retinal layer being imaged, there may not be any structural features to assist in registration of multiple images for averaging in order to improve the signal in the presence of weak fluorophores. Multimodal AO SLO and simultaneous AO OCT has been demonstrated, providing 3D location of features that are visible in both the fluorescence and backscattering detection [41]. However, since different light sources were used, 3D localization of the fluorophores was not possible for features that did not have an OCT signature.

This thesis presents a multi-modal imaging system using a single broadband light source combining cSLO and VIS-OCT, while using WSAO to correct ocular aberrations. This technology is developed for high resolution, non-invasive retinal imaging in the small animal eye. After aberration correction on the structural images with the WSAO engine, illumination using the same light source is able to excite fluorescent markers in the retina with high resolution, enabling simultaneous acquisition of fluorescence for depth resolved, molecule specific images that are perfectly registered to the 3D retinal structure.

1.5. Thesis Organization

The organization of the thesis is the following. Chapter 2 describes the background and theory of adaptive optics, and motivates the need for wavefront sensorless technology. Chapter 3 describes the system design for the multi-modal VIS-OCT and fluorescence imaging system used for data acquisition. Chapter 4 details the image acquisition parameters, and presents the results from both phantom and *in-vivo* data. Thesis conclusions are presented in Chapter 5 along with the discussion of potential future work.

Chapter 2. Adaptive Optics in Ophthalmic Imaging

This Chapter describes the details pertinent to adaptive optics theory. Direct measurement of the wavefront with a Shack-Hartmann wavefront sensor has been previously demonstrated for AO imaging in the small animal eye with excellent results [42]–[44], however this method can be challenging. Wavefront sensorless adaptive optics systems have been introduced to such areas to alleviate some of the limitations with direct wavefront sensing. This Chapter will discuss the background and theory of adaptive optics, the limitations associated with wavefront sensing in the small animal eye, and wavefront sensorless approaches in retinal imaging.

2.1. Overview of Adaptive Optics

Adaptive optics (AO) has roots in the field of astronomy. The technology was first developed in the 1950s because of the Earth's turbulent atmosphere causing distortion in light from astronomical sources, limiting the performance of ground-based telescopes [19]. AO was used to restore sharpness in the images by measuring and compensating for the distortions to the optical wavefront caused by the turbulence. AO technology has quickly advanced to achieve real-time correction for aberrations in wavefronts primarily through the use of Shack-Hartmann wavefront sensors and deformable mirrors.

In addition to the applications in astronomical imaging, adaptive optics is commonly used in optical microscopy and in ophthalmic imaging to dynamically compensate for optical aberrations. Aberrations arise from the sample being imaged due to inhomogeneous structures, and a mismatch of refractive indices at the corneal surface. Other sources of aberrations can be a result of the imaging system itself, depending on the quality of optical elements and alignment. Diffraction-limited focus is achieved when all light rays converge at a focal point with common phase. In the presence of aberrations, the direction and phase of light rays is modified so that they no longer focus at a common point, shown in Figure 4. The wavefront is distorted with aberrations, and no longer spherical. Aberrations in a sample inhibits a diffraction-limited focal spot, and limits the spatial resolution of an image. Adaptive optics is used to compensate for induced aberrations to restore a diffraction-limited focus, increasing the spatial resolution and contrast of features in an image.

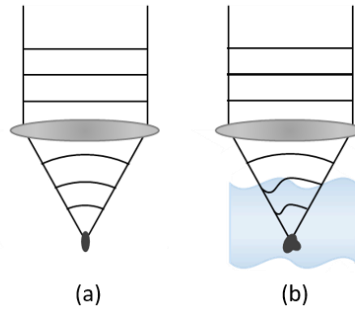


Figure 4: (a) Diffraction limited focus spot is achieved when there are no aberrations in a system or sample. (b) Focal spot is degraded due to aberrations in the sample.

There is a wide range of AO imaging systems suited to different applications with varying adaptive optical elements. Traditional components seen in AO systems include a Shack-Hartmann wavefront sensor, and an active optical element to shape the wavefront. Common approaches to wavefront sensing and wavefront correction are introduced in the following sections.

2.2. Wavefront Corrector

Compensation of sample aberrations can be achieved with active optical elements, including liquid crystal spatial light modulators, and deformable mirrors. Deformable mirrors can be classified into different classes based on their physical attributes. In this thesis, a segmented DM from Iris AO Inc. is used to shape the wavefront by varying the optical path length across the surface of the mirror. The PTT-111 from IrisAO is a high-performing DM that has been calibrated for precise linear open-loop positioning of the mirror segments. The mirror has 111 actuators underlying 37 piston-tip-tilt segments. The DM has 5 μm of stroke, capable of reaching tilt angles of ± 4 mrad. The update rate of the mirror segments can reach 2 kHz or greater.

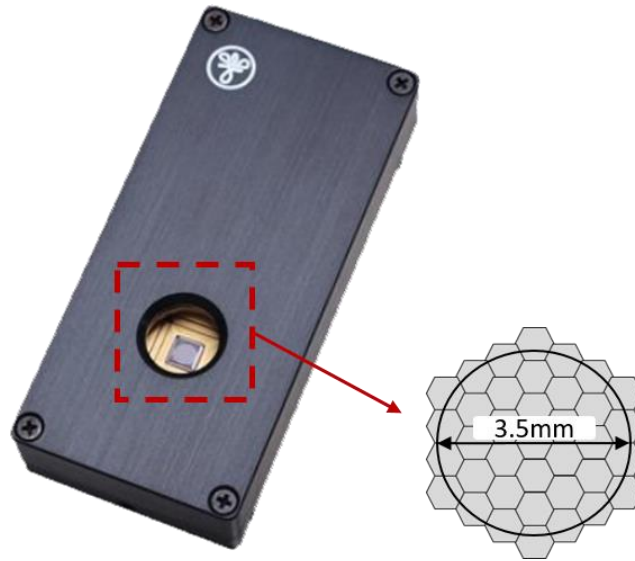


Figure 5: Segmented deformable mirror from IrisAO. [Credit: IrisAO, Inc.]

2.3. Wavefront Sensor

The Shack-Hartmann wavefront sensor is currently one of the most popular devices among wavefront sensors in the field of adaptive optics [19]. An array of lenslets with the same diameter and focal length are placed at a plane conjugate to the pupil plane. The SHWFS operates by measuring incident light through the lenslet array, which then passes onto a detector. The detector, typically a charge-coupled device (CCD) or complementary metal oxide semiconductor (CMOS) imager, uses groups of pixels as virtual sub-detection areas for wavefront measurement. When a planar wavefront is incident on the sensor, the foci of the beam are centered onto the according sub-detection areas. The image from the sensor is revealed as a perfect lattice of point images. In the presence of aberrations, the foci shift across the sensor (Figure 6). The local wavefront slopes are calculated by taking the ratio of the shift over the focal length of the lenslets, and the overall wavefront shape can be obtained by integration or by Zernike decomposition (discussed in Section 2.5.2).

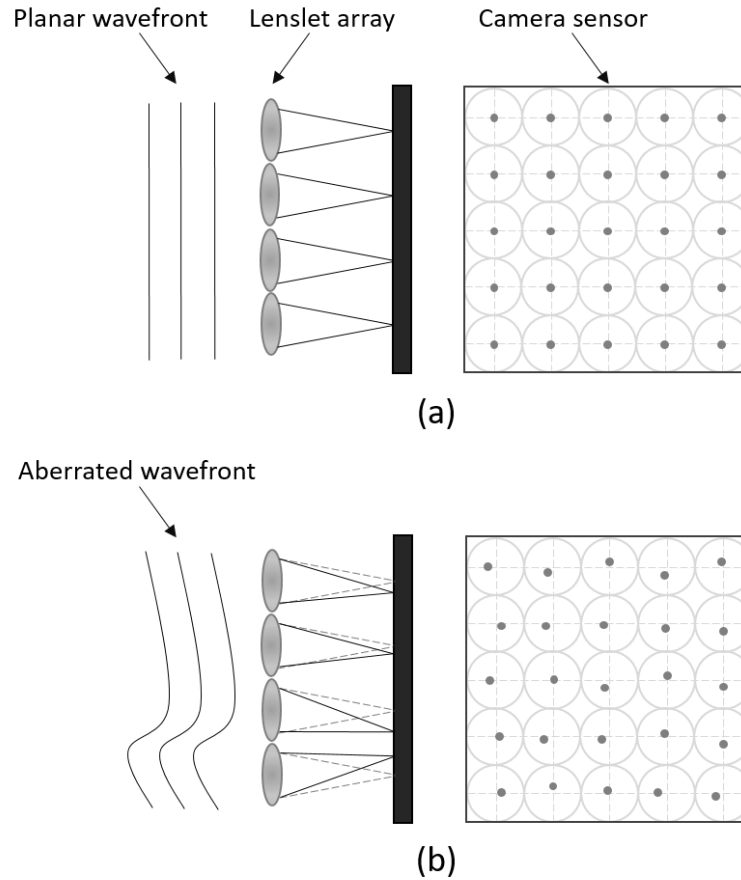


Figure 6: (a) A planar wavefront incident on the lenslet array produces a perfect lattice of point images. (b) An aberrated wavefront causes the focal spots to shift across the camera.

Direct wavefront sensing in adaptive optics can be advantageous since wavefront measurements can be performed with high-speed, which can be beneficial in cases where aberrations temporally vary. However, challenges arise in biological imaging, particularly with retinal imaging the small animal eye. Wavefront sensors can suffer from several problems including non-common path errors, and back-reflections from lenses. Additionally, Geng *et al.* discuss the ‘small-eye artifact’ [18]. The mouse retina appears to be optically thick because of the short effective focal length of the eye. As a result, light reflected from the retina produces radially elongated spot images on the wavefront sensor. An inferior spot quality introduces error in centroiding computations, affecting wavefront measurements and reconstruction. To minimize specular back reflections on the wavefront sensor, polarization optics can be used. However, to resolve

most limitations with direct wavefront sensing in the mouse eye, wavefront sensorless adaptive optics can be used as an alternative approach.

2.4. Polarization Optics

Polarization describes the orientation of the electric field oscillations which is perpendicular to the direction of propagation. Combinations of polarizing optical elements can be used to minimize back reflections from lenses seen by the wavefront sensor. In my previous work, I have incorporated polarization optics into a confocal scanning laser ophthalmoscopy imaging system. After the light source, a linear polarizer was used to confine the electric field of light to a single plane along the direction of propagation. Before the pupil plane, a quarter wave plate rotated at 45° was placed to convert the linearly polarized light to a state of circular polarization. Upon reflection from the sample, the handedness of the circular polarization was switched, which was then analyzed by a crossed linear polarizer in front of the wavefront sensor. With this configuration, any specular reflection from a lens would be rejected by the linear polarizer in front of the wavefront sensor as it was perpendicular to the polarization state emitted from the sample. In addition to removing back reflections from a wavefront sensor, the same configuration of polarizing elements was used with confocal SLO imaging. Results of this work are demonstrated as part of my contributions at the end of the thesis.

2.5. Wavefront Sensorless Adaptive Optics

2.5.1. Image Optimization

Rather than directly measuring a wavefront, wavefront sensorless adaptive optics indirectly deduces aberrations from a set of image measurements. Wavefront sensorless AO has been previously demonstrated in both human and mouse with excellent results [30], [34], [35], [42]–[44]. The optimization algorithm used in this thesis is the hill-climbing modal search [48] to determine the optimal Zernike coefficient value for each mode. Evenly spaced incremental step sizes of coefficients are applied to each Zernike mode sequentially. The optimal coefficient is then determined by a merit function, which characterizes the image by attributes such as sharpness. An aberrated wavefront is then reconstructed as a sum of the weighted orthogonal basis functions, which in this case

are the Zernike polynomials. Following the search for the optimized value of each Zernike coefficient, the deformable mirror is set with the wavefront shape that follows the equation:

$$w(\mathbf{k}) = \sum_{n=3}^N k_n Z_n \quad \text{Eq. 2-4}$$

where w_k is the wavefront shape, k is a vector of Zernike coefficients, and N is the number of modes that have been optimized. Zernike modes 1 through 3 (piston, tip, tilt) are set to zero as they use mirror stroke to create geometrical distortions to the image, but do not affect resolution or signal intensity [19]. A flow chart summarizing the modal search algorithm is shown in Figure 7.

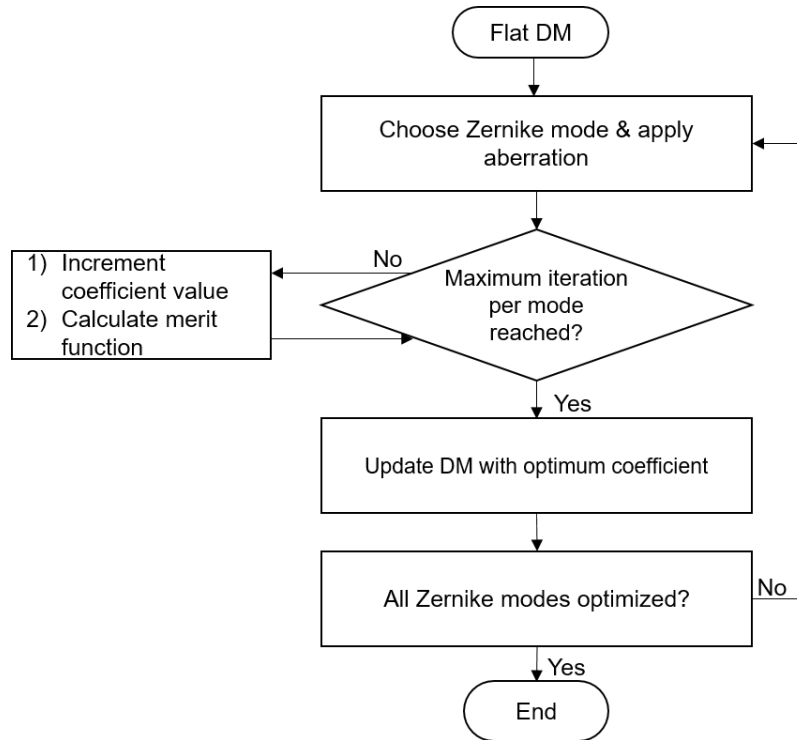


Figure 7: Flow chart of the hill-climbing modal search algorithm.

2.5.2. Zernike Polynomials

Zernike polynomials are a set of orthogonal polynomials that are defined over the unit circle satisfying the following equation:

$$Z_n^m(r, \theta) = \begin{cases} m < 0 : \sqrt{2}R_n^{-m}(r)\sin(-m\theta) \\ m = 0 : 0 \\ m > 0 : \sqrt{2}R_n^m(r)\cos(m\theta) \end{cases} \quad \text{Eq. 2-1}$$

where indices n and m are even, and restricted to the conditions $n - |m|$ and $n \geq |m|$ [19]. $R_n^m(r)$ are radial polynomials defined as:

$$R_n^m(r) = \sqrt{n+1} \sum_{s=0}^{(n-m)/2} \frac{(-1)^s (n-s)!}{s! \left(\frac{n+m}{2} - s\right)! \left(\frac{n-m}{2} - s\right)!} r^{n-2s} \quad \text{Eq. 2-2}$$

The property of orthogonality allows for an aberrated wavefront to be decomposed into a weighted sum of Zernike polynomials that are independent of one another. The decomposition of an aberration function, $\Psi(r, \theta)$, can then be defined as the following:

$$\Psi(r, \theta) = \sum_{i=1}^{\infty} M_i Z_i(r, \theta) \quad \text{Eq. 2-3}$$

where M_i represents the modal coefficients describing the amplitude of each Zernike polynomial, $Z_i(r, \theta)$ [19]. Table 1 lists the aberration terms of the Zernike modes, and Figure 8 demonstrates the shapes of each mode up to the 4th radial order.

Index (j)	Radial order (n)	Angular frequency (m)	Aberration term
1	0	0	Piston
2	1	1	Tip
3	1	-1	Tilt
4	2	0	Defocus
5	2	-2	Oblique astigmatism
6	2	2	Vertical astigmatism
7	3	-1	Vertical coma
8	3	1	Horizontal coma
9	3	-3	Vertical trefoil
10	3	3	Oblique trefoil
11	4	0	Primary spherical
12	4	2	Vertical secondary astigmatism
13	4	-2	Oblique secondary astigmatism
14	4	4	Vertical quadrafoil

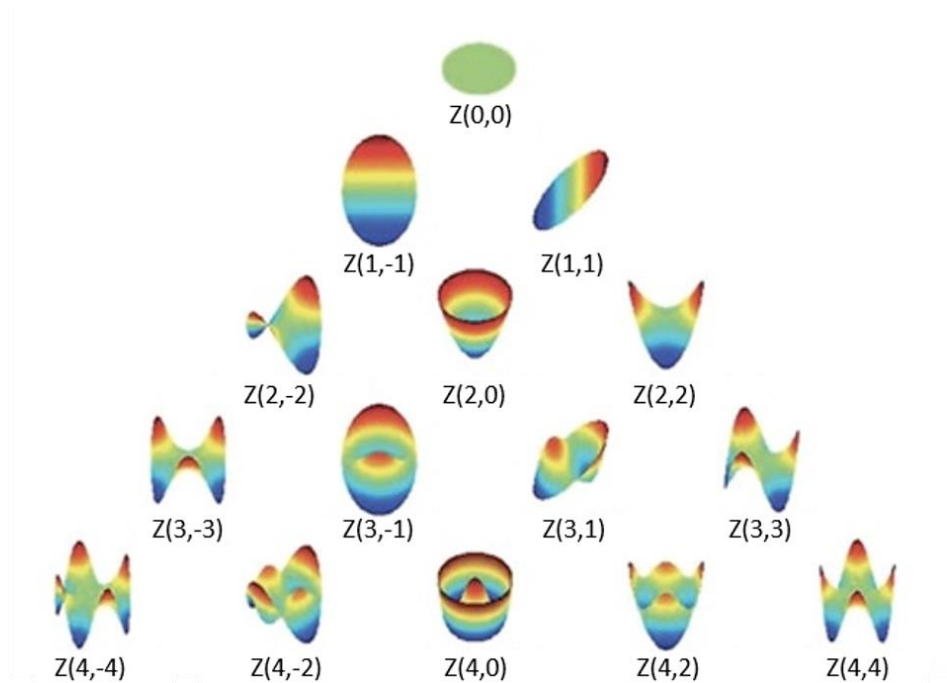


Figure 8: Zernike polynomials ordered vertically by radial degree.

2.6. Depth Resolved Image-Guided WSAO

A nice feature of AO-OCT is that the axial and lateral resolution are decoupled from one another. The axial resolution is dependent on the spectral bandwidth of the source, whereas the lateral resolution is dependent on the NA of the imaging optics. In commercial OCT systems using NIR light, the Rayleigh range is on the order of a hundred micrometers, with a corresponding spot size on the order of 20 μm . This spot size is inadequate for resolving photoreceptors [49]. Although the retina is thicker than the Rayleigh range of AO-OCT imaging systems, the retinal layers outside the depth of focus can still be visualized if the imaging depth and sensitivity of the OCT is adequate.

SHWFS based AO systems are insensitive to the depth variations of aberrations. The low NA of each individual beam from the lenslet array is insensitive to the axial position in which the signal originates from. In contrast, depth resolved image-guided aberration correction uses the anatomical features of the retinal layers for optimization. Because OCT detects coherence-gated ballistic photons with high SNR, aberration correction can be performed even when images are low in intensity. In cases where the accuracy of a wavefront measurement is limited (for example increased opacity in the

eye, or cataracts), WSAO OCT can potentially be used to obtain high-resolution images. Additionally, OCT provides cross-sectional images of the retina, and a layer of interest can be selected in real time for aberration correction. Other imaging modalities, such as cSLO, can also be used for image-guided depth resolved aberration correction. High-speed WSAO aberration correction has been demonstrated in 2D *en-face* images of the retina [47]. However, the disadvantage is that cSLO has inferior axial optical sectioning capability compared to OCT, and requires relatively planar structures for optimization.

2.7. Summary

In this Chapter, the theory of adaptive optics is introduced. Shack-Hartmann wavefront sensing AO has been previously demonstrated for mouse retinal imaging, however this method can be challenging. Removing the wavefront sensor, aberrations can be deduced indirectly using a computational algorithm. The following Chapter discusses simultaneous visible light optical coherence tomography and fluorescence imaging, integrated with wavefront sensorless adaptive optics to correct aberrations from the mouse eye. The experimental setup is described in Chapter 3.

Chapter 3. Methods

The system in this thesis is for simultaneous depth-resolved WSAO and single photon fluorescence that has been adapted to retinal imaging applications. The fluorescence imaging is combined with depth-resolved VIS-WSAO-OCT using a supercontinuum visible light source, while using separate detection systems. In the case of weak fluorescent signal, the coherence-gated, depth resolved VIS-OCT images can be used for image-guided WSAO aberration correction. However, if the sample expresses strong fluorophores, the fluorescent signal can be used as a guide-star for VIS-OCT optimization. This Chapter discusses the VIS-OCT and fluorescence system topology, and delineates the differences between traditional NIR-OCT and VIS-OCT.

3.1. System Characterization

3.1.1. Axial Resolution

The axial resolution of an OCT system is determined by the spectral bandwidth of the light source, defined by the following equation:

$$l_c = \frac{2 \cdot \ln(2) \lambda_0^2}{\pi \Delta\lambda} \quad \text{Eq. 3-1}$$

To measure the axial resolution, a common-path interferometer, shown in Figure 9, was configured to minimize the dispersion mismatch between reference and sample arm, and from imperfect fiber coupler splitting.

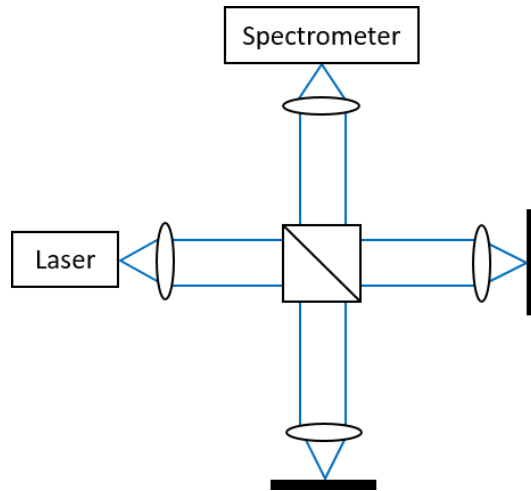


Figure 9: Schematic of a common path interferometer used to measure the axial resolution. Light is emitted from the source, split into two arms by a 50/50 beam splitter, then recombined at the spectrometer.

The axial resolution was measured as the full width half maximum (FWHM) of the point spread function (PSF). The measured resolution was then compared to the theoretical axial resolution, which is inversely proportional to the bandwidth of the source. Table 2 summarizes the results of the theoretical and measured resolution.

Table 2: Summary of theoretical and measured axial resolution

λ_0	$\Delta\lambda$	Theoretical Resolution	Measured Resolution
560 nm	50 nm	2.8 μm	3.4 μm

3.1.2. Sensitivity

To measure the sensitivity of the VIS-OCT system, a fiber-based Michelson interferometer was configured. A dispersion compensation block was placed in the reference arm to match the dispersion in the sample arm to avoid broadening of the PSF. A mirror was placed at the end of the sample arm, and the power coupled back to the detector was maximized. To avoid saturation of the signal from the sample arm, a calibrated neutral density filter was used. Figure 10 demonstrates the configuration of the system that was used to calculate the sensitivity.

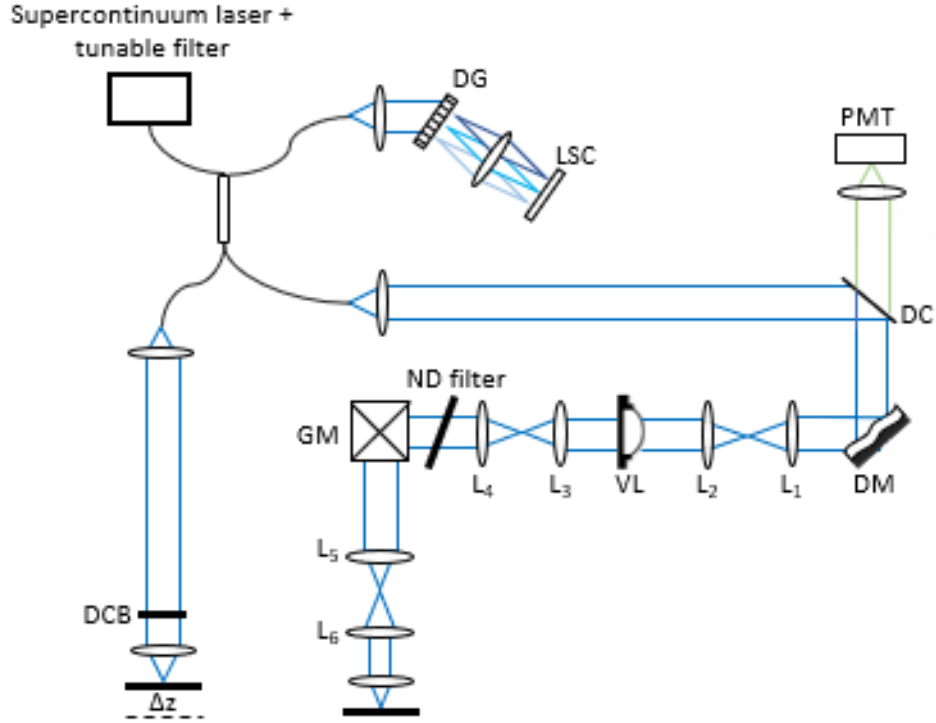


Figure 10: System used to calculate SNR and sensitivity roll-off. A mirror is placed at the end of each arm. The reference arm is translated by a distance of Δz , with a dispersion compensation block (DCB) to match the sample arm. A neutral density (ND) filter is placed in the sample arm to avoid saturation on the line scan camera (LSC).

Initial retinal imaging experiments were intended to be used with a center wavelength of 560 ± 25 nm, thus the sensitivity measurements were performed using the same wavelength and bandwidth. The measured sensitivity was calculated using the following equation [50]:

$$SNR_{cal}(dB) = 20 \cdot \log_{10} \left(\frac{PeakAscan}{\sigma_{noise}} \right) + Calibrated Losses \quad Eq.3-2$$

where σ_{noise} is the standard deviation of the noise, and the calibrated losses include power loss through the optical system, as well as from the neutral density filter.

The measured sensitivity was then compared to the theoretical sensitivity, which is defined with the equation [50]:

$$SNR_{theoretical}(dB) = \frac{P_s \cdot R_s \cdot \rho \cdot \Delta t}{e}$$

where P_s is the power reflected from the sample arm, R_s is the reflectivity of the sample arm, ρ is the responsivity of the detector, Δt is the exposure time of the camera, and e is the electronic charge. The theoretical and measured sensitivity results are summarized in Table 3.

Table 3: Summary of theoretical and measured SNR

P_{sample}	Δt	ρ	Theoretical Sensitivity	Measured Sensitivity
285 μW	50 μs	0.21 A/W	102 dB	88 dB

To calculate the sensitivity roll-off, measurements from the sample arm were taken every 50 μm over 1.6 mm. The 3dB fall off point was at 0.7 mm, and the roll-off curve is shown in Figure 11.

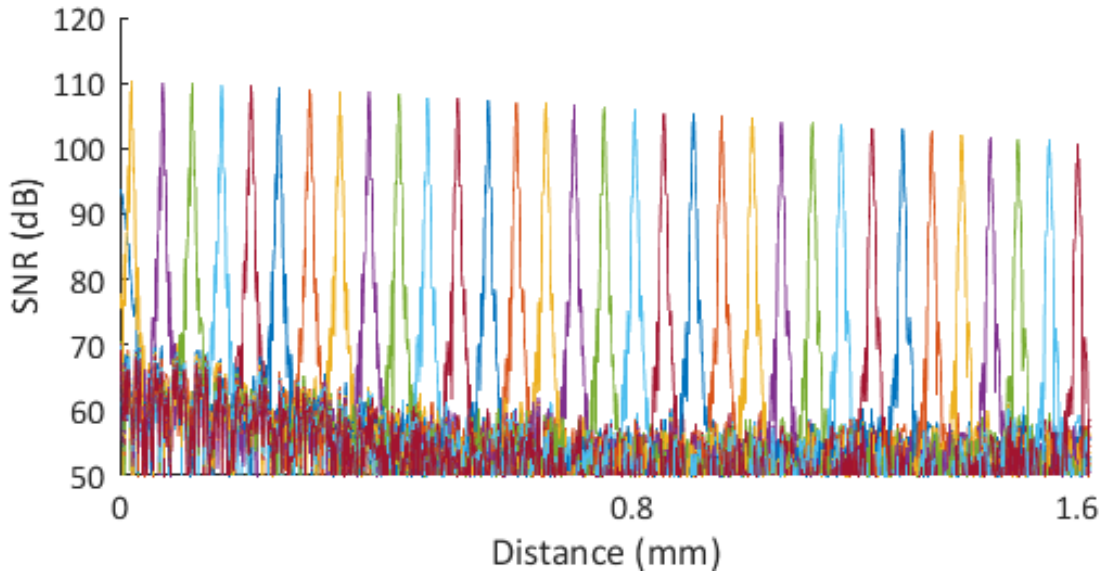


Figure 11: Sensitivity roll-off curve.

3.2. System Design

3.2.1. System Topology

The light source for the multi-modal imaging system was a supercontinuum laser from NKT Photonics (Fianium WhiteLase Micro). The broad spectral range of the source

covers 400 – 2000 nm, with a total output power of ~500mW, and pulse repetition rate of 30 MHz. To select the desired wavelength, a tunable single line filter was used (SuperK Varia). Multiple system configurations were tested. Initial experiments for phantom imaging used a center wavelength of 470 nm. However, with strong attenuation of the lower wavelengths with the 460 HP fiber, a center wavelength of 560 ± 25 nm was used for VIS-OCT imaging at a low NA. The final implementation of the imaging system was configured for OCT using 560 ± 15 nm, and fluorescence excitation using 470 nm. The output from the filter was fiber coupled to a single mode fiber, which was then connected to a 50/50 560nm wideband 460-HP fiber coupler. The reference arm was implemented in a cat's eye configuration, with a dispersion compensation block consisting of H-ZLAF52 glass. The sample arm consisted of excitation light guided to the segmented deformable mirror (PTT-111, IrisAO Inc.) for aberration correction, then relayed to a variable focus lens (Arctic 39N0, Varioptics) to control the focal plane in the sample. A telescope was used to relay the beam to the galvanometer-scanning mirrors (6210H, Cambridge Technology Inc.) to scan the light across the sample. The beam was guided through the final telescope to the sample with a beam diameter of 0.7 mm. The corresponding numerical aperture (NA) was 0.18 for mouse retinal imaging. A schematic of the system is shown in Figure 12 and Figure 13.

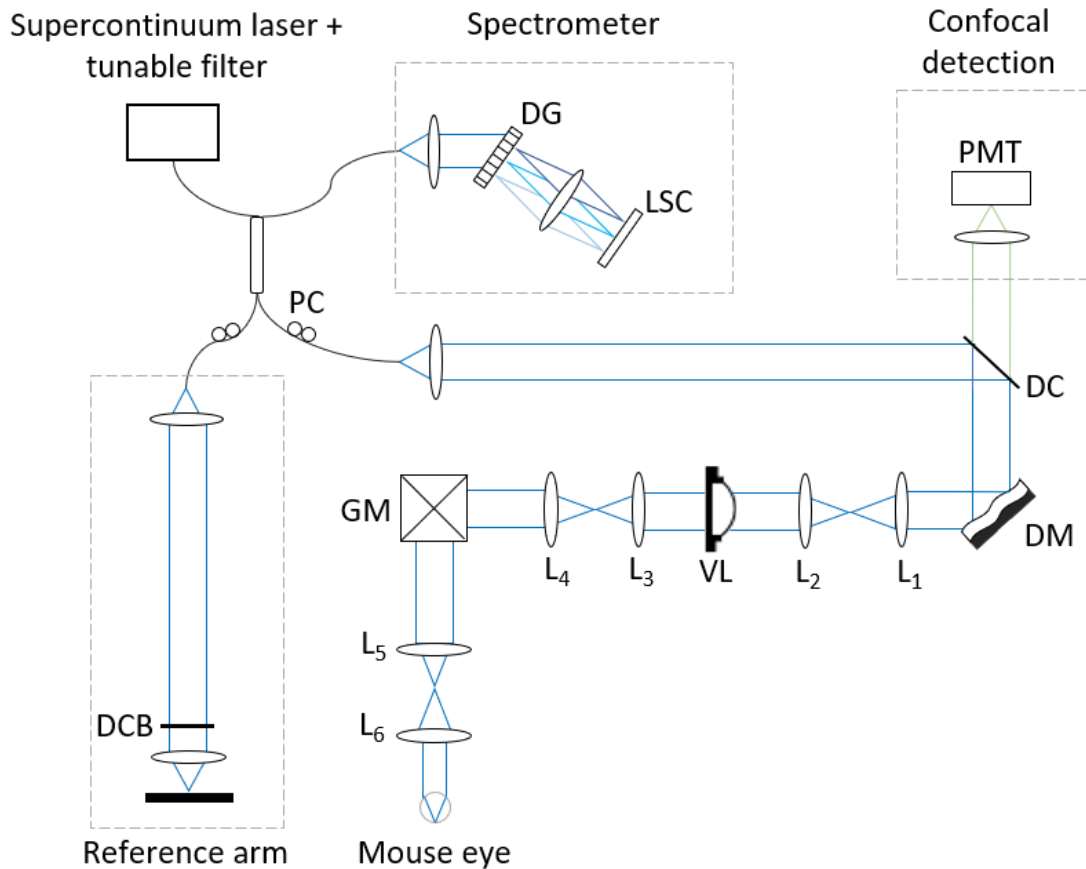


Figure 12: Multimodal VIS-OCT and fluorescence imaging system. Light emitted from the supercontinuum source is coupled into a single mode 50/50 fiber coupler with a polarization controller (PC) in the reference and sample arm. Light passes through a dichroic mirror (DC), then to the DM. $\{L_1, L_2, L_3, L_4\} = \{200\text{m}, 200\text{mm}, 150\text{mm}, 100\text{mm}\}$. Light is scanned over the retina with the galvanometer mirrors (GM). $\{L_5, L_6\} = \{100\text{mm}, 30\text{mm}\}$. The reference arm is implemented in a cat's-eye configuration, with a dispersion compensation block (DCB). Back scattered light is detected with the spectrometer, consisting of a diffraction grating (DG) and line scan camera (LSC). Fluorescence is detected with the confocal detection channel, using a photomultiplier tube (PMT) as the detector.

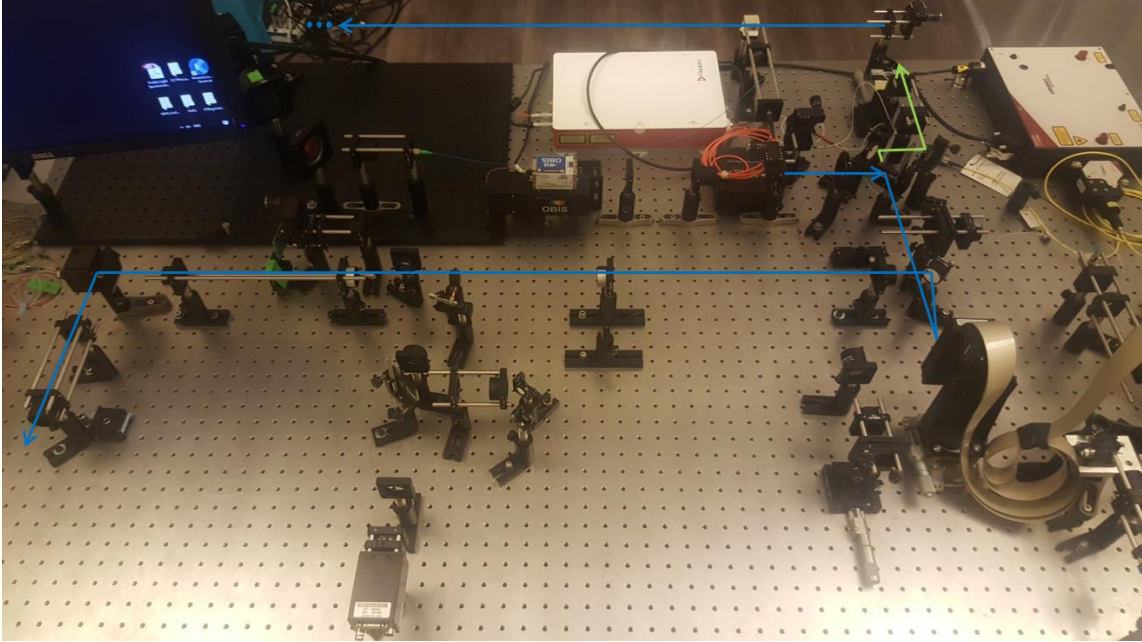


Figure 13: Image of the multimodal VIS-OCT and fluorescence imaging system.

The back-scattered excitation light was recombined with the reference arm light at the fiber coupler. The light from both sample and reference arms generated an interference pattern on the spectrometer, which was designed using a 4k pixel Basler Sprint linear array detector and a visible light transmissive grating with 1800l/mm (WP-1800/532, Wasatch Photonics). Real time cross-sectional images were processed using a custom GPU-accelerated program [51]. The A-scan rate was configured at 40kHz, resulting in an acquisition rate of 1 volume per second with acquisition parameters of 2048 x 200 x 200 sample points.

The fluorescence emission from the sample was transmitted through a multi-edge filter (89402bs, Chroma Technology). A clean up filter (89402m, Chroma Technology) was used to reject any residual excitation and back-scattered light from the sample, and a lens and pinhole were used to reject out-of-focus light with a confocal aperture ~ 6.5 times the Airy disk. A photomultiplier tube (PMT) was used as the detector with a frequency bandwidth of 200kHz. The photosensor module contained an internal low-noise transimpedance amplifier to convert the current output to a voltage output. The digitization of the PMT was synchronized to the acquisition of the VIS-OCT A-scans to ensure that both the OCT and fluorescence images were perfectly registered. OCT-guided WSAO optimization was first performed using the *en-face* image, followed by

switching the imaging system to the fluorescence mode. Using a sinusoidal bidirectional scan pattern, fluorescence images were acquired with 200 x 200 samples at a frame rate of 10 frames per second.

3.2.2. Longitudinal Chromatic Aberrations

Chromatic aberrations arise from the wavelength-dependence on the refractive index of the optical lenses in an imaging system. This effect, known as longitudinal chromatic aberrations (LCA), results in a spectral decomposition of broadband light. Through experimental work, it was noticed that aspheric lenses caused strong chromatic aberrations. The inability to focus light at the same axial position resulted in narrowing of the source spectrum, shown in Figure 14.

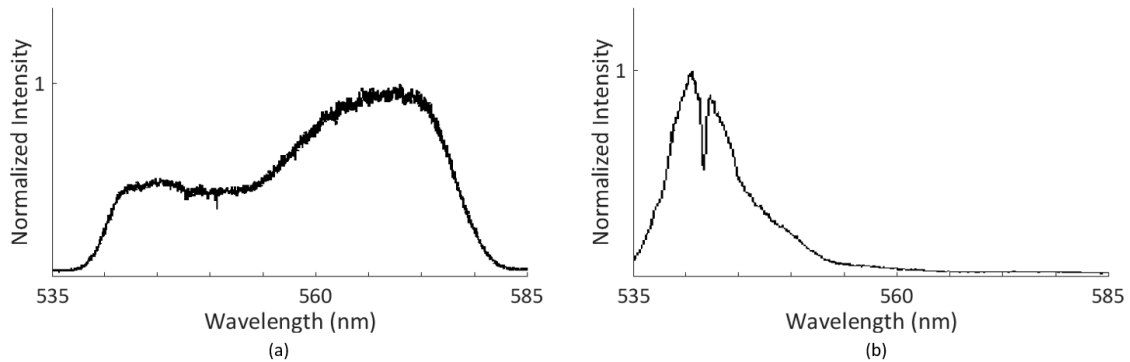


Figure 14: (a) Source spectrum using only achromatic lenses in the system. (b) Aspheric lenses cause chromatic aberrations, resulting in narrowing of the source spectrum.

The axial point spread function in an OCT imaging system is the inverse Fourier transform of the source spectrum, known as the coherence function [50]. Narrowing of the source spectrum due to LCA results in broadening of the PSF, degrading the axial resolution. Thus, all lenses used in the VIS-OCT imaging system were off-the-shelf A-coat achromat doublets. Achromat lenses generally consist of two different types of glass cemented together with a concave and convex radius of curvature to compensate for longitudinal chromatic aberrations [19].

3.2.3. Spectrometer Design and Calibration

The detection channel for the spectral domain VIS-OCT system was a spectrometer, which was designed and simulated with Zemax by former BORG member, Mr. Ryne Watterson. The spectrometer, designed to measure the intensity of the interferometric signal as a function of wavelength, consisted of a 60mm air-spaced achromatic doublet collimating lens, a transmissive diffraction grating with 1800l/mm, a 200mm focusing lens consisting of two achromatic doublet lenses stacked together, and a CMOS line-scan camera (Basler SPL 4096-140km). The spectrometer was designed in the Littrow configuration, where the incident and diffracted angles of light are the same to achieve optimal grating efficiency. The grating equation in the Littrow configuration is as follows:

$$2\sin\theta_l = Gm\lambda \quad \text{Eq. 3-4}$$

where θ_l is the Littrow configuration angle, G is the groove density of the grating, m is the order of diffraction, and λ is the center wavelength of the source. The angular dispersion was calculated to find the number of pixels over which the 50nm bandwidth of light covers. The equation for the angular dispersion, D , is:

$$D = \frac{\partial\theta}{\partial\lambda} = \frac{Gm}{\cos\theta_l} \quad \text{Eq. 3-5}$$

Each pixel in the line scan Basler camera is 10 μ m. The 50nm bandwidth of light covered 2062 pixels, corresponding to a spectral resolution of 0.024nm/pixel. The spectrometer configuration is shown in Figure 15. Alignment of the spectrometer was performed as part of the experimental work of this thesis.

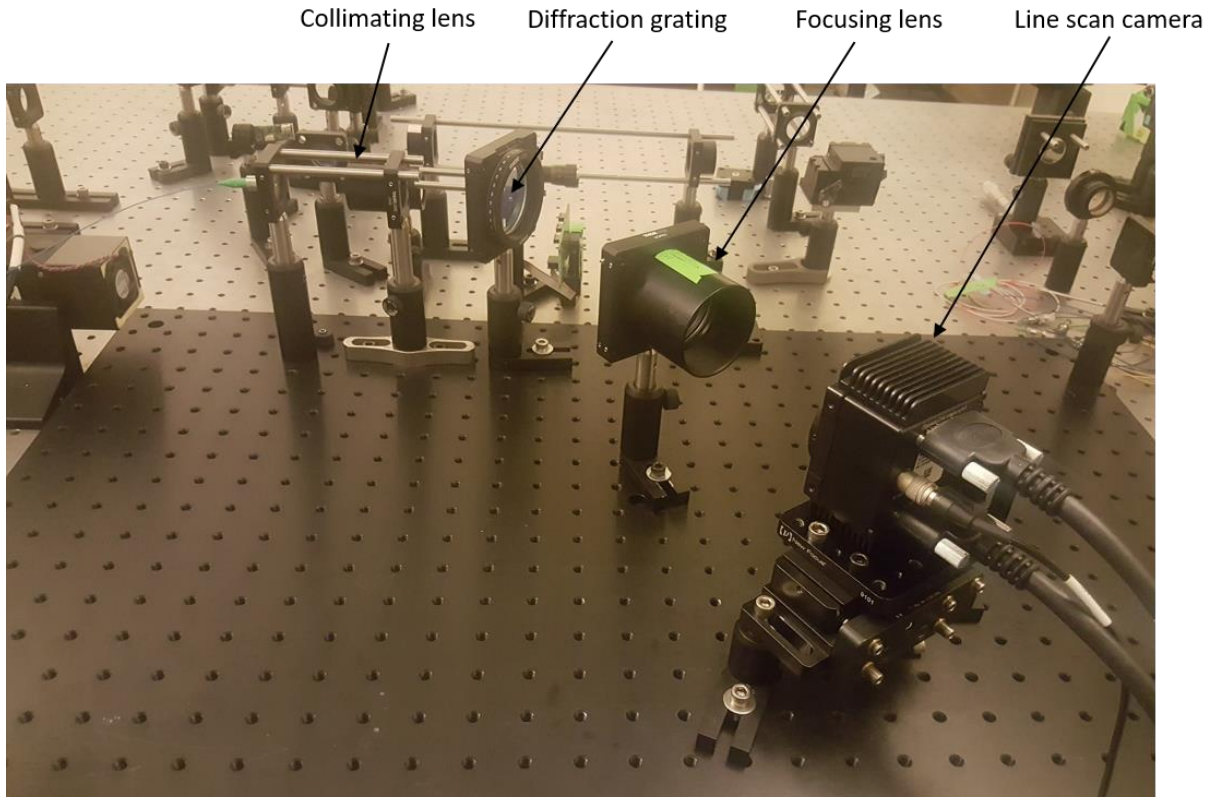


Figure 15: Spectrometer used in the detection channel of the VIS-OCT system.
 $\{f_{\text{collimator}}, f_{\text{focusing}}\} = \{60\text{mm}, 200\text{mm}\}.$

Before Fourier transforming data captured from the spectrometer, the data must be resampled uniformly in wavenumber to achieve optimal axial resolution. Rescaling the data was computed by BORG member, Dr. Myeongjin Ju. Interferograms were captured using the common path interferometer shown in Figure 9. The unwrapped phase values of the spectral fringes were extracted from the calibration signal, and the pixel number as a function of wavenumber was fitted by a polynomial of rank r . The corresponding curve was used to determine interpolation points prior to the inverse Fourier transform.

3.3. Summary

This Chapter presents the AO VIS-OCT and fluorescence imaging system. The dual-mode imaging system is capable of performing simultaneous depth-resolved structural imaging as well as molecular contrast imaging. The benefits of using a single light source for two imaging modalities is that the complexity of post-processing the

images is reduced because there is no need to correlate the OCT and fluorescence images; they are acquired perfectly co-registered with one another. Furthermore, using a single light source can reduce the exposure time of the light on the retina if the acquisition of fluorescence and OCT is simultaneous. The following Chapter presents the results obtained from the VIS-OCT and fluorescence imaging system.

Chapter 4.

In this chapter, the results of the VIS-OCT and fluorescence imaging in the mouse retina *in-vivo* are presented. VIS-OCT is demonstrated in phantom imaging using a center wavelength of 470nm, and *in-vivo* using a center wavelength of 560nm. Imaging with VIS-OCT at different numerical apertures is demonstrated, and fluorescence images following VIS-OCT optimization are shown.

4.1. Mouse Handling

Wild-type C57BL/6J and EGFP-labelled ganglion cell B6 Cg-Tg(Thy1-EGFP)MJrs/J mice were obtained from Jackson Laboratories (Bar Harbor, ME, USA), which were used for imaging in this thesis. The mice were imaged with the approval of the University Animal Care Committee at Simon Fraser University while following the protocols compliant to the Canadian Council on Animal Care. The mice were anesthetized with a subcutaneous injection of ketamine (100 mg/kg of body weight) and dexmedetomidine (0.1 mg/kg of body weight) prior to the imaging session. Following the injection, the eyes were dilated with a drop of topical solution (Tropicamide, 1%). A contact lens (Cantor & Nissel Ltd, UK) was then applied to protect the cornea from dehydration. The anesthetized mouse was placed on a translation stage and aligned to the final lens of the system without contact, and the laser power at $\sim 110 \mu\text{m}$. After the experiment, the recovery of the mice was induced with an injection of atipamezole (1.8 mg/kg of body weight).

4.2. Adaptive Optics Image Acquisition Parameters

4.2.1. Image Acquisition

The A-scan rate of the VIS-OCT system for *in-vivo* imaging was configured to 40 kHz. The volume size during optimization was 2048 x 200 x 50, resulting in a volume rate of 4 volumes/second. Five radial modes were corrected during the optimization, corresponding to 18 Zernike modes. Searching 11 steps per mode, the optimization time was ~ 50 seconds 5 radial orders. The optimization was performed on the *en-face* images, which were generated by maximal intensity projection along the depth of a

selected region in a B-scan. The merit function, M , used for optimization is defined as the following:

$$M = \frac{\sum I_j^2}{(\sum I_j)^2} \quad \text{Eq. 4-1}$$

where I_j is the intensity value of the j -th pixel in the OCT *en-face* image, and the summation is performed over the entire image.

Following the optimization of the OCT image, the system was switched to the fluorescence channel. For simultaneous optimization of structural and functional images, the pinhole in the fluorescence confocal detection channel was positioned axially to ensure the fluorescence was near the same retinal layer of the OCT image. The fluorescence images were acquired with 200 x 200 sample points at a rate of 10 frames/second with the DM on before and after aberration correction.

4.2.2. Image Processing

Raw OCT data was processed into axial scans by a Fourier transformation. Resampling the A-scans from wavelength to wavenumber was performed using a look up table. The dispersion was matched between both reference and sample arm, so numerical dispersion compensation was not needed. To correct for sample motion, axial correction along the B-scans was performed by Fourier based cross-correlation rigid registration. *En-face* images were then generated by manually selecting a region in the B-scan, and averaging along the selected depth. A non-rigid cubic B-spline registration algorithm with a sum of squared differences similarity metric was used for non-rigid registration of the *en-face* images, which was provided by Matlab's Medical Image Registration Toolbox.

The fluorescence images were processed by converting raw binary files into 2-D images. Rigid registration was performed by Fourier based cross-correlation, followed by averaging of frames to increase the SNR.

4.3. Results

4.3.1. Phantom Imaging

Initial imaging experiments were performed using a center wavelength of 470 nm. The goal was to perform VIS-OCT at this wavelength and simultaneous functional imaging using enhanced green fluorescent protein (EGFP). EGFP is a fluorophore that's readily available in many different transgenic mouse models, and expresses strong fluorescent signal. Using the blue light, phantom imaging was performed with an NA of 0.23. The phantom model consisted of lens tissue fibers labeled with fluorescein. Aberrations were created by placing a gel between two non-uniform plastic surfaces. The results are presented in Figure 16.

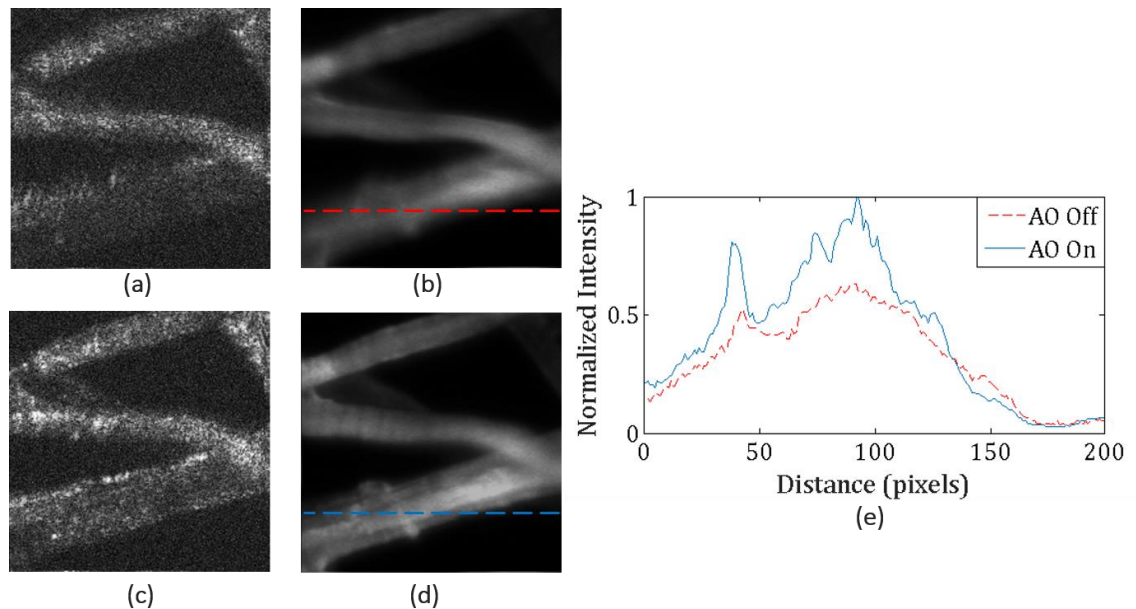


Figure 16: (a),(b) *En-face* OCT and fluorescence images before aberration correction and (c),(d) after correction. (e) Line spread function taken across the dashed lines demonstrating the performance of the correction.

In-vivo experiments using $\lambda_0 = 470$ nm were unsuccessful, as shorter wavelengths in the visible light spectrum are attenuated in the 460 HP fiber [11], and the power of the source is inherently lower. The OCT *in-vivo* experiments were thus performed with $\lambda_0 = 560$ nm, which are presented in the remainder of this Chapter.

4.3.2. VIS-OCT Low Numerical Aperture Imaging

A low NA of 0.1 was initially used for retinal imaging with VIS-OCT. These results were obtained with a 470 wideband fiber coupler, which reduced the power coupled back to the detector. Figure 17 shows a single frame B-scan and an average of 100 frames, and Figure 18 shows a single frame B-scan and an average of 200 frames at a wider field of view, demonstrating the decrease in SNR because of the sparse sampling.

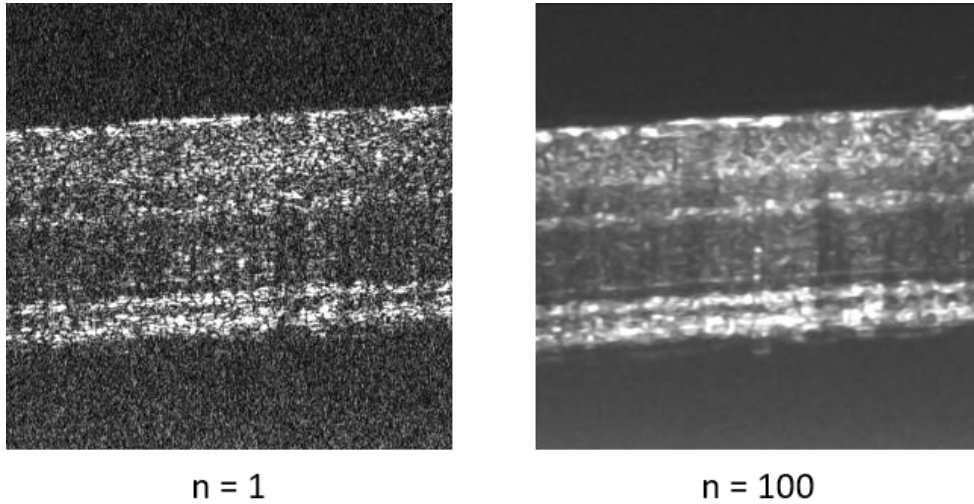


Figure 17: Left: Single frame B-scan. Right: An average of 100 B-scans.

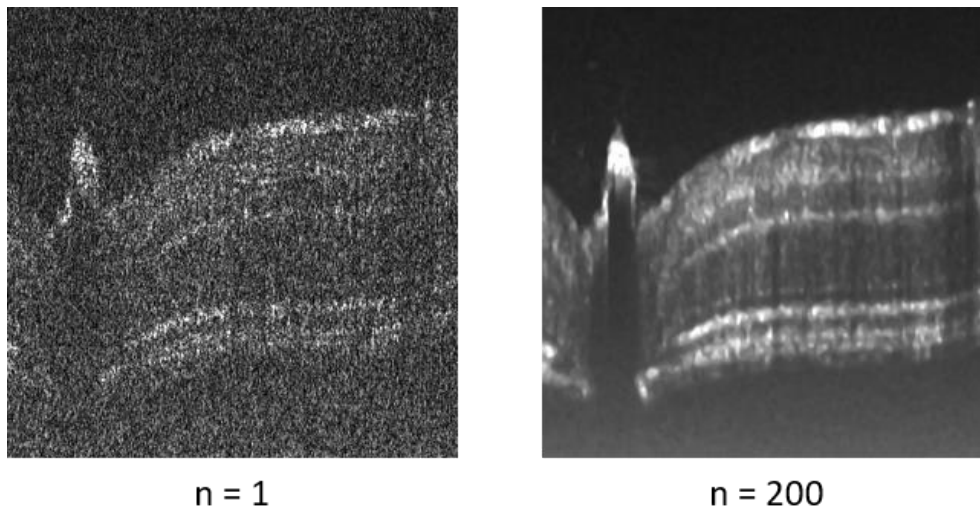


Figure 18: Left: Single frame B-scan. Right: An average of 200 B-scans.

The NA was incrementally increased to 0.15 prior to AO imaging, and the fiber was switched to a 560 wideband 50/50 coupler, increasing the SNR of the images with more light coupled back to the detector. A volume was acquired with the focus at the nerve fiber layer (NFL), and the B-scan and *en-face* view are shown in Figure 19.

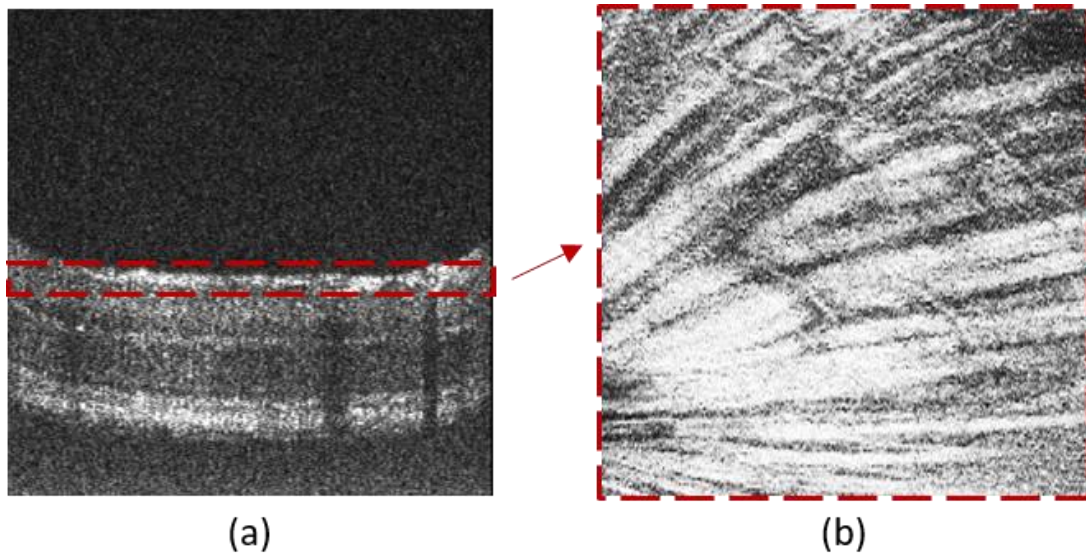


Figure 19: (a) B-scan (b) En-face image of the NFL. Each image is an average of 3 frames.

4.3.3. *In-vivo* AO VIS-OCT and Fluorescence Imaging

Thus far, VIS-OCT was successful using a center wavelength of 560 nm. The limitation with using this wavelength, however, is that there are not many mouse models expressing red fluorescent protein within the retina. The solution to this limitation was to switch the dichroic mirror to a multi-edge filter (89402bs, Chroma Technology), permitting OCT optimization at 560 nm, and fluorescence excitation at 470 nm. The numerical aperture was increased to 0.18 for AO VIS-OCT. A fluorescein angiography in a wild type mouse was performed, and Figure 20 demonstrates optimization that was performed on the NFL layer, then focused down to the outer plexiform layer (OPL) to image the capillaries with the fluorescence channel.

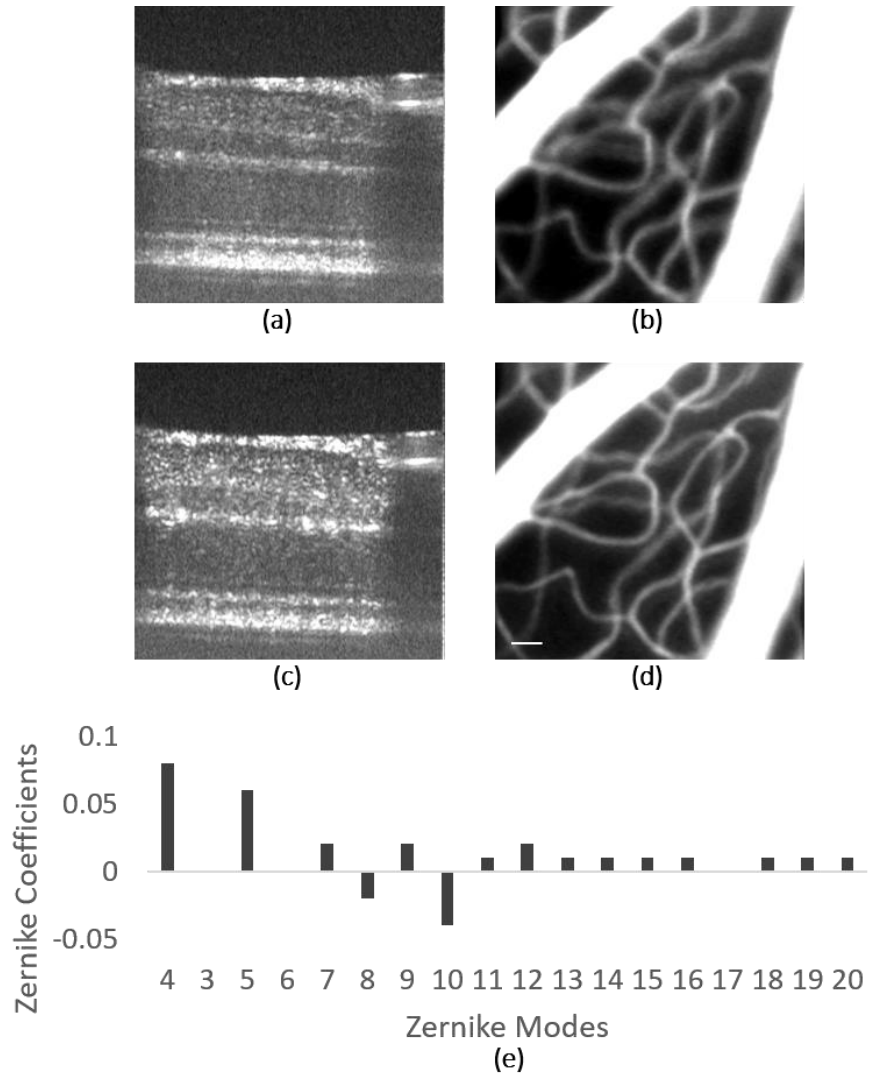


Figure 20: (a),(b) OCT B-scan and fluorescein angiography before optimization and (c),(d) after aberration correction. Scale bar, 30 μm . (e) The Zernike coefficients selected during the optimization are demonstrated.

A mouse with ganglion cells labelled with EGFP was then imaged. Again, the optimization was performed on the NFL layer of the OCT image on a small field of view of $\sim 250 \mu\text{m}$. Following the optimization, the field of view was zoomed out, and the wavelength was switched to 470 nm to excite the labelled EGFP cell. The results are shown in Figure 21.

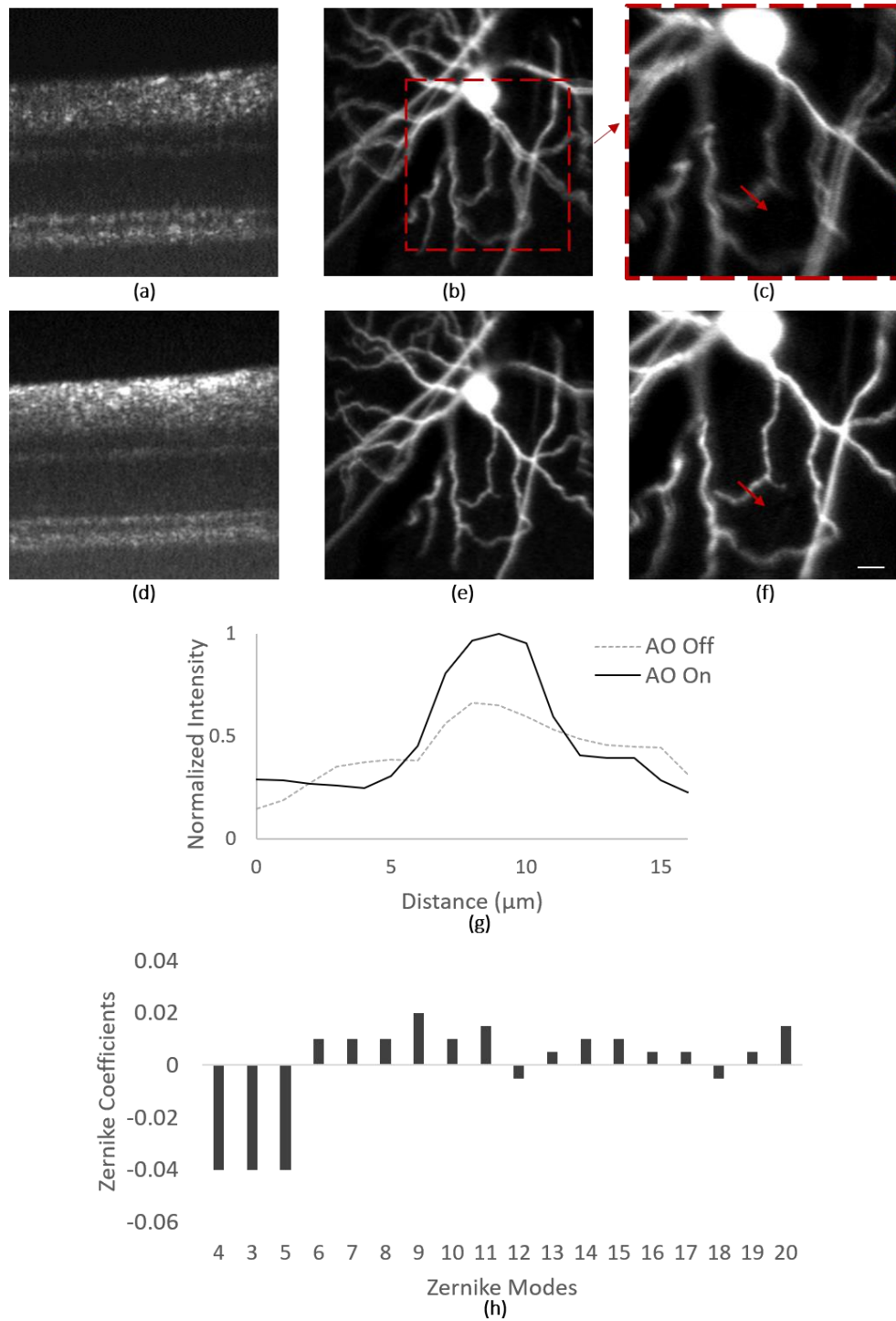


Figure 21: (a),(b),(c) B-scan and EGFP labelled ganglion cell before optimization, and (d),(e),(f) the optimized images. Scale bar, 30 μm . (g) The line spread function taken across the arrows labelled in (c) and (f). (h) The Zernike coefficients selected during optimization are demonstrated.

4.4. Discussion

Visible light OCT is advantageous compared to traditional NIR OCT due to the inherent higher axial and lateral resolutions. The drawback however, is the reduced depth of focus (DOF). With VIS-AO-OCT, there is a pronounced trade-off between NA and DOF. Initial AO experimentations were performed with an NA of 0.3 in the mouse retina. The corresponding depth of focus ($\sim 29\mu\text{m}$) was too short, reducing the SNR of the total B-scan, as well as the *en-face* view. Since image-based adaptive optics is dependent on the initial starting image, the optimization doesn't perform if there are no retinal anatomical features in the image to optimize, or if the starting point is too poor due to the low SNR. Thus, the NA was reduced to 0.18 for the AO-VIS-OCT imaging system.

Although VIS-OCT with blue light has been demonstrated by other research groups such as [6] and [13], the results using a center wavelength of 470nm for the retina were unsuccessful in this thesis. The main difference between the experimental setups was the light source. The maximum power achieved at the sample using 470nm was $<200\ \mu\text{W}$ (SuperK Whitelase Micro), whereas VIS-OCT in [6] and [13] used more than twice this power (SuperK EXU3). Using a different light source, such as the SuperK EXU3, would allow the opportunity to perform VIS-OCT with blue light and fluorescence imaging of proteins that are readily available in a wide variety of transgenic mouse models.

Switching to 560nm for VIS-OCT provided images with higher SNR compared to 470nm, however the trade-off was that there are not many mouse models that express red fluorescent protein in the retina. As a compromise, optimization of the OCT image was performed at 560nm, then switched to 470nm for fluorescence imaging of enhanced yellow fluorescent protein and/or enhanced green fluorescent protein. Rather than optimizing the signal path for the excitation, the optimization was for the fluorescence wavelength range. The benefit of this approach was that the fluorophore didn't photobleach while optimizing the OCT, and multiple wavelengths could be used for fluorescence excitation. This approach enabled low power imaging at multiple wavelengths that are well below the maximum permissible exposure for the mouse eye.

Chapter 5. Future Work

5.1. VIS-OCT for Retinal Oximetry

VIS-OCT has recently gained attention because of its capability to quantify retinal blood oxygen saturation rate (sO_2). sO_2 is defined as the percentage of hemoglobin binding sites that are occupied by oxygen molecules. Previous methods to measure sO_2 include multiwavelength fundus photography. The distinct different absorption spectrum of deoxygenated hemoglobin (Hb) and oxygenated hemoglobin (HbO_2) are used to calculate optical densities of retinal vessels and estimate sO_2 . However, fundus photography is limited by blood cell scattering, variations in vessel diameter, and fundus pigmentation absorption [14]. The fundamental limit of fundus photography, is that optical signals from outside or inside blood vessels are inseparable because of the lack of axial resolution.

VIS-OCT is suitable for measuring sO_2 compared to fundus photography and NIR-OCT. The absorption of blood in the NIR light range is very weak, and so applications *in-vivo* cannot be performed. In addition to the improved lateral and axial resolutions, the optical absorption of hemoglobin has strong contrast using VIS-OCT. VIS-OCT can give an sO_2 measurement with high accuracy because the coherent detection minimizes influences from surrounding tissues. Additionally, since NIR-OCT is the gold standard in ophthalmic clinics, adding VIS-OCT as a functional imaging tool can be quickly adopted in clinics.

Methods to quantify sO_2 have been demonstrated by Zhang *et al.* [14]. In brief, their proposed algorithm is based on the assumption that the bottom of a blood vessel wall can be imaged with high SNR. The reflected spectrum of light is extracted by a series of short-time Fourier transforms. sO_2 is calculated by a least-squares fit of the spectroscopic VIS-OCT intensity to the known attenuation spectra of deoxygenated and oxygenated whole blood. The challenge with this approach is that larger blood vessels ($>130 \mu\text{m}$) strongly attenuate light because of the longer optical path, and small capillaries ($\sim 10 \mu\text{m}$) have low optical absorption. However, their work has been demonstrated in vessels with diameters between 30-130 μm with sufficient SNR.

Retinal blood oxygen saturation rate has previously been an overlooked measurement because of the lack of accurate methods for quantification. With easy adoption in ophthalmic clinics, VIS-OCT has potential to diagnose the pathophysiology of vision disorders including age related macular degeneration, and diabetic retinopathy with quantitative sO_2 measurements.

5.2. VIS-OCT WSAO by Pupil Segmentation

In this thesis, a hill-climbing modal search algorithm was used for aberration correction. The limitation to image-based optimization methods is that they require many frames to calculate the value of an image metric, and result in a long optimization time. This can be challenging for *in-vivo* applications, where respiratory motion and movement from patients can hinder the optimization. Reducing the time required for sensorless-based optimization methods becomes a goal to transition adaptive optics for *in-vivo* retinal imaging to applications in vision science. An alternative method of WSAO that uses the acquired images to indirectly measure the wavefront aberrations in the sample could potentially be used with VIS-OCT, known as pupil segmentation adaptive optics (PSAO).

PSAO measures a wavefront using images acquired with different segments of the imaging pupil to determine the gradient of the wavefront at each pupil location. In the case where no aberrations are present, all of the rays across the pupil of the imaging system will converge at the sample to a focal spot size limited only by diffraction. However, in the presence of aberrations, the heterogeneity in the index of refraction and imperfections in the shape of the ocular structures will deflect the rays in the different segments across the pupil to different lateral positions at the focal plane. PSAO measures the deflection of the beam at each pupil segment with respect to a reference image, commonly selected as the central portion of the pupil, in order to determine the local wavefront tilt at that pupil segment. A set of images is acquired with different segments of the beam, called ‘target beamlets’, and the wavefront gradient at each region of the pupil is determined by measuring the shift in the image with respect to the reference. These indirect measurements of the wavefront slope using PSAO are conceptually similar to the output of a SHWFS. The aberrations are corrected by shaping the deformable mirror into the phase conjugate of the measured wavefront. The PSAO method has been demonstrated with great success for by Ji *et al.* for *in-vivo* mouse brain

imaging [15–18], which encourages the extension of this AO method to *in-vivo* retinal imaging modalities.

PSAO for VIS-OCT would require some considerations. For *in-vivo* applications, motion from the sample can introduce an image shift that impedes the measurement of the local wavefront slopes. To minimize the effect of motion, the image acquisition process can be modified to collect a reference image in rapid succession with each target image. Additionally, the acquisition can alternate between reference and target beamlets within a frame to further mitigate the effect of motion. The A-scan rate of the AO VIS-OCT engine would need to be increased to rapidly acquire images for this approach to PSAO, but at the expense of the decrease in sensitivity. However, PSAO for VIS-OCT would be a promising optimization approach that can rapidly correct aberrations for *in-vivo* applications.

5.3. VIS-OCT with Multi-Fluorescence Imaging

Using a supercontinuum light source provides the opportunity to do VIS-OCT with multi-fluorescence imaging using different excitation wavelengths. Transgenic mice expressing different fluorophores in the retina can be imaged with different spectral bands to visualize different cells and features within the same field of view. Using a multi-edge dichroic filter permits fluorescence excitation and detection at multiple wavelengths. With multi-fluorescence imaging, selection of fluorophores with a Stoke's shift that corresponds to the bands of the multi-edge filters can be a design constraint. Another limitation is that a smaller bandwidth of the excitation light must be used to remain within the bands of the multi-edge filter. The limited source bandwidth reduces the axial resolution of the VIS-OCT, and the power delivered to the eye. The latter can potentially be resolved with using a different supercontinuum source with higher power, such as the SuperK EXU3 from NKT Photonics.

Contributions

In addition to the thesis work, I have also worked on other projects with the Biomedical Optics Research Group. One of my projects was focused in developing a different wavefront sensorless aberration correction algorithm, known as pupil segmentation adaptive optics (PSAO). PSAO was developed for *in vivo* mouse retinal imaging using a fluorescence confocal scanning laser ophthalmoscopy imaging system, with the results published in [55], and shown in Figure 22 and Figure 23.

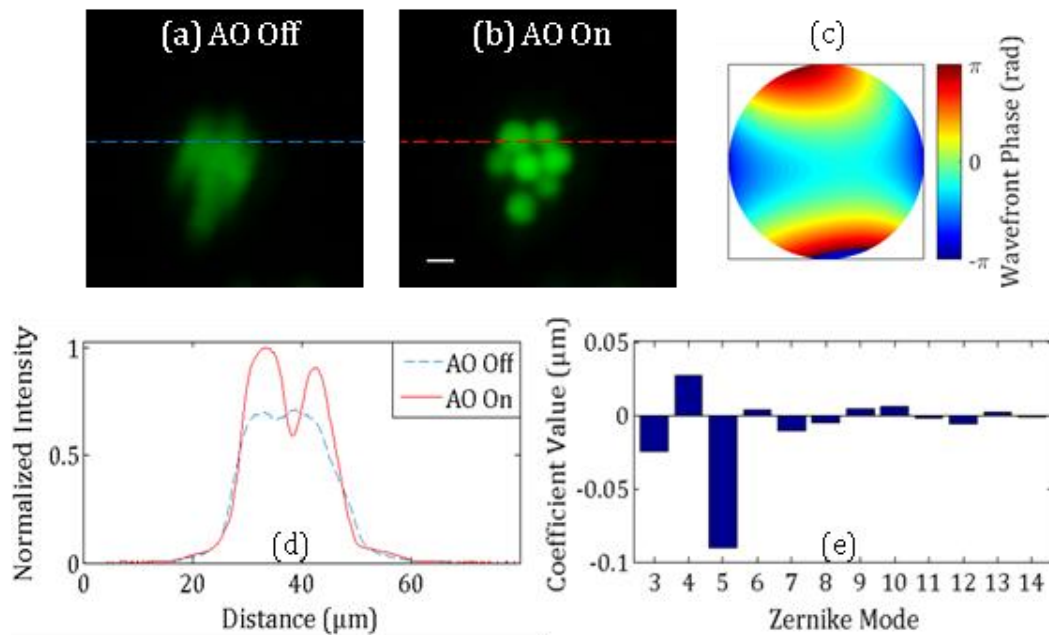


Figure 22: 6 μm fluorescent beads with aberration correction (AO on) and without (AO off). (a) and (b) are an average of 30 frames. Scale bar, 6 μm . (c) Wavefront aberration map. (d) Normalized intensity at the dashed lines indicating a $\sim 30\%$ increase. (e) Zernike coefficients for the corrected wavefront.

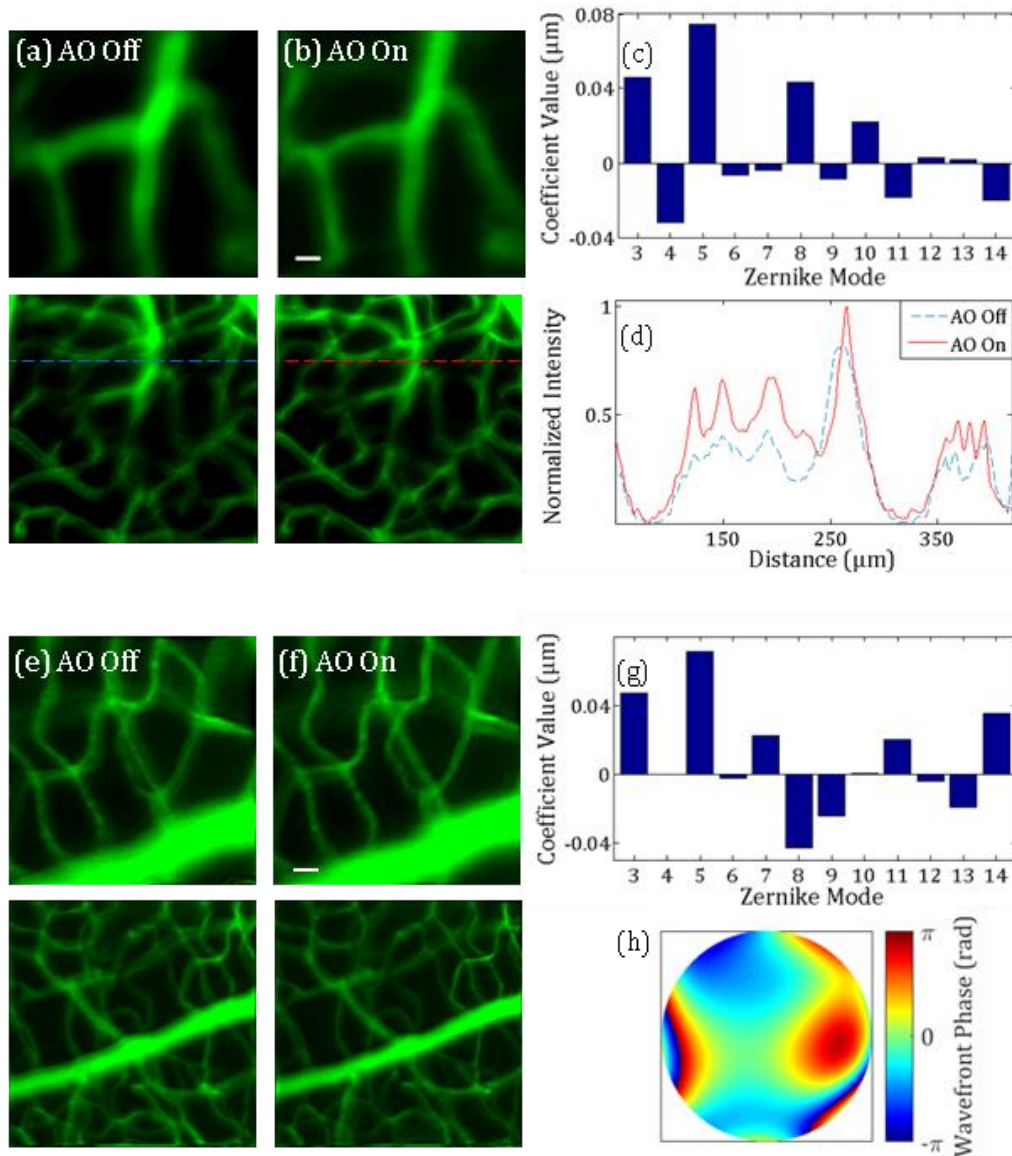


Figure 23: (a,b,e,f) PSAO for retinal fluorescein angiography with aberration correction (AO on) and without (AO off) for two mice. Scale bars, 20 μm . (c,g) Zernike coefficients for the corrected wavefront. (d) The normalized intensity at the location of the dashed lines had a $\sim 30\%$ increase in the peak intensity after correction. (h) The wavefront aberration map for the bottom panel.

As mentioned in Chapter 2, I also worked on a project involving polarization optics to remove back reflections from wavefront sensors, as well as reflectance imaging. Figure 24 demonstrates the results, with a small back reflection introduced from the quarter wave plate (which can be removed by rotating the element slightly off axis). Figure 25 demonstrates simultaneous SLO and fluorescein angiography imaged with the same laser source at the same location in the retina.

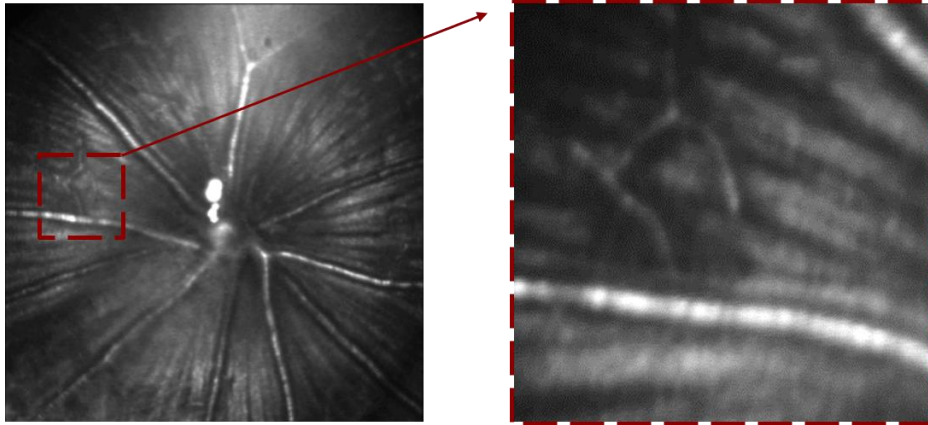


Figure 24: SLO images acquired using polarization optics to remove specular reflections from lenses.

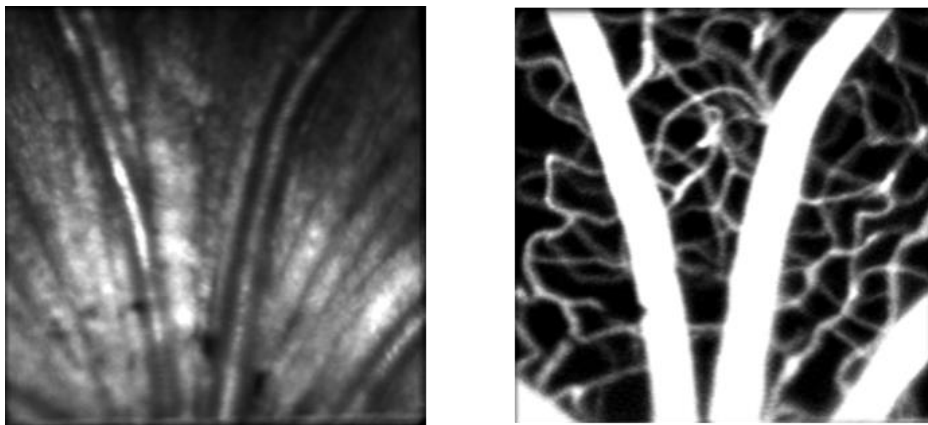


Figure 25: SLO and fluorescence imaging acquired at the same location using the same light source.

Finally, a manuscript has been prepared for submission containing my contributions from the thesis work with wavefront sensorless adaptive optics VIS-OCT and fluorescence imaging.

References

- [1] C. L. Rowe-Rendleman *et al.*, “Drug and gene delivery to the back of the eye: from bench to bedside,” *Invest. Ophthalmol. Vis. Sci.*, vol. 55, no. 4, pp. 2714–30, Apr. 2014.
- [2] M. Garcia Garrido, S. C. Beck, R. Mühlfriedel, S. Julien, U. Schraermeyer, and M. W. Seeliger, “Towards a quantitative OCT image analysis.,” *PLoS One*, vol. 9, no. 6, p. e100080, Jan. 2014.
- [3] S. Kumar, Z. Berriochoa, A. D. Jones, and Y. Fu, “Detecting abnormalities in choroidal vasculature in a mouse model of age-related macular degeneration by time-course indocyanine green angiography.,” *J. Vis. Exp.*, no. 84, p. e51061, Jan. 2014.
- [4] B. C. Chauhan *et al.*, “Longitudinal in vivo imaging of retinal ganglion cells and retinal thickness changes following optic nerve injury in mice.,” *PLoS One*, vol. 7, no. 6, p. e40352, Jan. 2012.
- [5] X. Shu, L. Beckmann, and H. F. Zhang, “Visible-light optical coherence tomography: a review,” *J. Biomed. Opt.*, vol. 22, no. 12, p. 1, Dec. 2017.
- [6] Z. Nafar, M. Jiang, R. Wen, and S. Jiao, “Visible-light optical coherence tomography-based multimodal retinal imaging for improvement of fluorescent intensity quantification.,” *Biomed. Opt. Express*, vol. 7, no. 9, pp. 3220–3229, Sep. 2016.
- [7] S. Chen, J. Yi, and H. F. Zhang, “Measuring oxygen saturation in retinal and choroidal circulations in rats using visible light optical coherence tomography angiography,” *Biomed. Opt. Express*, vol. 6, no. 8, p. 2840, Aug. 2015.
- [8] R. McNabb, T. Blanco, D. Saban, J. Izatt, and A. Kuo, “Single Source Fluorescence Imaging/Blue Optical Coherence Tomography in a GFP Mouse Model,” in *ARVO Annual Meeting*, 2014.
- [9] S. P. Chong, C. W. Merkle, C. Leahy, H. Radhakrishnan, and V. J. Srinivasan, “Quantitative microvascular hemoglobin mapping using visible light spectroscopic Optical Coherence Tomography,” *Biomed. Opt. Express*, vol. 6, no. 4, p. 1429, Apr. 2015.
- [10] S. Chen, X. Shu, P. L. Nesper, W. Liu, A. A. Fawzi, and H. F. Zhang, “Retinal oximetry in humans using visible-light optical coherence tomography [Invited],” *Biomed. Opt. Express*, vol. 8, no. 3, p. 1415, Mar. 2017.
- [11] S. P. Chong, M. Bernucci, H. Radhakrishnan, and V. J. Srinivasan, “Structural and functional human retinal imaging with a fiber-based visible light OCT ophthalmoscope,” *Biomed. Opt. Express*, vol. 8, no. 1, p. 323, Jan. 2017.

- [12] P. L. Nesper, B. T. Soetikno, H. F. Zhang, and A. A. Fawzi, "OCT angiography and visible-light OCT in diabetic retinopathy," *Vision Res.*, vol. 139, pp. 191–203, 2017.
- [13] C. Dai, X. Liu, and S. Jiao, "Simultaneous optical coherence tomography and autofluorescence microscopy with a single light source.," *J. Biomed. Opt.*, vol. 17, no. 8, pp. 80502–1, Aug. 2012.
- [14] J. Yi, Q. Wei, W. Liu, V. Backman, and H. F. Zhang, "Visible-light optical coherence tomography for retinal oximetry.," *Opt. Lett.*, vol. 38, no. 11, pp. 1796–8, Jun. 2013.
- [15] J. Yi, S. Chen, V. Backman, and H. F. Zhang, "In vivo functional microangiography by visible-light optical coherence tomography," *Biomed. Opt. Express*, vol. 5, no. 10, p. 3603, Sep. 2014.
- [16] R. N. Pittman, "In vivo photometric analysis of hemoglobin.," *Ann. Biomed. Eng.*, vol. 14, no. 2, pp. 119–37, 1986.
- [17] Y. Geng *et al.*, "In vivo imaging of microscopic structures in the rat retina.," *Invest. Ophthalmol. Vis. Sci.*, vol. 50, no. 12, pp. 5872–9, Dec. 2009.
- [18] Y. Geng *et al.*, "Optical properties of the mouse eye," *Biomed. Opt. Express*, vol. 2, no. 4, pp. 717–738, 2011.
- [19] J. A. Kubby, *Adaptive Optics for Biological Imaging*. CRC Press, 2013.
- [20] J. Porter, H. Queener, J. Lin, K. Thorn, and A. A. S. Awwal, *Adaptive Optics for Vision Science: Principles, Practices, Design and Applications (Wiley Series in Microwave and Optical Engineering)*. Wiley-Interscience.
- [21] R. Tyson, *Adaptive Optics Engineering Handbook*, vol. 1999. CRC Press, 1999.
- [22] S. Remtulla and P. E. Hallett, "A schematic eye for the mouse, and comparisons with the rat," *Vision Res.*, vol. 25, no. 1, pp. 21–31, Jan. 1985.
- [23] C. Schmucker and F. Schaeffel, "A paraxial schematic eye model for the growing C57BL/6 mouse.," *Vision Res.*, vol. 44, no. 16, pp. 1857–67, Jan. 2004.
- [24] E. G. de la Cera, G. Rodríguez, L. Llorente, F. Schaeffel, and S. Marcos, "Optical aberrations in the mouse eye.," *Vision Res.*, vol. 46, no. 16, pp. 2546–53, Aug. 2006.
- [25] D. P. Biss, R. H. Webb, Y. Zhou, T. G. Bifano, P. Zamiri, and C. P. Lin, "<title>An adaptive optics biomicroscope for mouse retinal imaging</title>," in *MOEMS-MEMS 2007 Micro and Nanofabrication, 2007*, pp. 646703-646703–8.
- [26] D. P. Biss *et al.*, "In vivo fluorescent imaging of the mouse retina using adaptive optics.," *Opt. Lett.*, vol. 32, no. 6, pp. 659–61, Mar. 2007.

- [27] C. Alt, D. P. Biss, N. Tajouri, T. C. Jakobs, and C. P. Lin, "An adaptive-optics scanning laser ophthalmoscope for imaging murine retinal microstructure," *Proc. SPIE*, vol. 7550, p. 7555019, Feb. 2010.
- [28] X. Zhou, P. Bedggood, and A. Metha, "Limitations to adaptive optics image quality in rodent eyes.," *Biomed. Opt. Express*, vol. 3, no. 8, pp. 1811–24, Aug. 2012.
- [29] M. J. Booth, "Wavefront sensorless adaptive optics for large aberrations," *Opt. Lett.*, vol. 32, no. 1, pp. 5–7, Jan. 2007.
- [30] M. J. Booth, "Adaptive optical microscopy: the ongoing quest for a perfect image," *Light Sci. Appl.*, vol. 3, no. 4, p. e165, Apr. 2014.
- [31] A. Jesacher and M. J. Booth, "Sensorless adaptive optics for microscopy," in *Adaptive Optics for Biological Imaging*, S. S. Olivier, T. G. Bifano, and J. A. Kubby, Eds. 2011, pp. 177–190.
- [32] H. Hofer, N. Sredar, H. Queener, C. Li, and J. Porter, "Wavefront sensorless adaptive optics ophthalmoscopy in the human eye," *Opt. Express*, vol. 19, no. 15, pp. 14160–14171, Jul. 2011.
- [33] D. J. Wahl *et al.*, "Wavefront sensorless approaches to adaptive optics for in vivo fluorescence imaging of mouse retina," in *SPIE BiOS*, 2016.
- [34] N. Ji, D. E. Milkie, and E. Betzig, "Adaptive optics via pupil segmentation for high-resolution imaging in biological tissues," *Nat. Methods*, vol. 7, no. 2, pp. 141–147, Feb. 2010.
- [35] A. Roorda, F. Romero-Borja, I. Donnelly, H. Queener, T. Hebert, and M. Campbell, "Adaptive optics scanning laser ophthalmoscopy," *Opt. Express*, vol. 10, no. 9, pp. 405–412, May 2002.
- [36] D. R. Williams, "Imaging single cells in the living retina," *Vision Res.*, vol. 51, no. 13, pp. 1379–1396, Jul. 2011.
- [37] A. Roorda, "Adaptive optics for studying visual function: a comprehensive review.," *J. Vis.*, vol. 11, no. 7, Jan. 2011.
- [38] B. Hermann *et al.*, "Adaptive-optics ultrahigh-resolution optical coherence tomography," *Opt. Lett.*, vol. 29, no. 18, p. 2142, Sep. 2004.
- [39] Y. Zhang, J. Rha, R. S. Jonnal, and D. T. Miller, "Adaptive optics parallel spectral domain optical coherence tomography for imaging the living retina," *Opt. Express*, vol. 13, no. 12, p. 4792, Jun. 2005.
- [40] J. Liang, D. R. Williams, and D. T. Miller, "Supernormal vision and high-resolution retinal imaging through adaptive optics," *J. Opt. Soc. Am. A*, vol. 14, no. 11, p. 2884, Nov. 1997.

- [41] R. J. Zawadzki *et al.*, “Adaptive-optics SLO imaging combined with widefield OCT and SLO enables precise 3D localization of fluorescent cells in the mouse retina,” *Biomed. Opt. Express*, vol. 6, no. 6, pp. 2191–2210, Jun. 2015.
- [42] J. Schallek, Y. Geng, H. Nguyen, and D. R. Williams, “Morphology and Topography of Retinal Pericytes in the Living Mouse Retina Using In Vivo Adaptive Optics Imaging and Ex Vivo Characterization,” *Invest. Ophthalmol. Vis. Sci.*, vol. 54, no. 13, pp. 8237–8250, Dec. 2013.
- [43] Y. Geng *et al.*, “Adaptive optics retinal imaging in the living mouse eye,” *Biomed. Opt. Express*, vol. 3, no. 4, pp. 715–734, Apr. 2012.
- [44] Y. Jian, R. J. Zawadzki, and M. V. Sarunic, “Adaptive optics optical coherence tomography for *in vivo* mouse retinal imaging,” *J. Biomed. Opt.*, vol. 18, no. 5, p. 56007, May 2013.
- [45] D. P. Biss, R. H. Webb, Y. Zhou, T. G. Bifano, P. Zamiri, and C. P. Lin, “An adaptive optics biomicroscope for mouse retinal imaging,” in *Proceedings of SPIE*, 2007, vol. 6467, no. 1, p. 646703.
- [46] X. Zhou, P. Bedggood, B. Bui, C. T. O. Nguyen, Z. He, and A. Metha, “Contrast-based sensorless adaptive optics for retinal imaging,” *Biomed. Opt. Express*, vol. 6, no. 9, pp. 3577–3595, Sep. 2015.
- [47] D. J. Wahl, Y. Jian, S. Bonora, R. J. Zawadzki, and M. V Sarunic, “Wavefront sensorless adaptive optics fluorescence biomicroscope for *in vivo* retinal imaging in mice,” *Biomed. Opt. Express*, vol. 7, no. 1, pp. 1–12, Jan. 2016.
- [48] Y. Jian, J. Xu, M. A. Gradowski, S. Bonora, R. J. Zawadzki, and M. V. Sarunic, “Wavefront sensorless adaptive optics optical coherence tomography for *in vivo* retinal imaging in mice,” *Biomed. Opt. Express*, vol. 5, no. 2, pp. 547–559, Feb. 2014.
- [49] Y. Jian *et al.*, “Lens-based wavefront sensorless adaptive optics swept source OCT,” *Sci. Rep.*, vol. 6, no. 1, p. 27620, Sep. 2016.
- [50] W. Drexler and J. G. Fujimoto, *Optical coherence tomography: technology and applications*. .
- [51] Y. Jian, K. Wong, and M. V Sarunic, “Graphics processing unit accelerated optical coherence tomography processing at megahertz axial scan rate and high resolution video rate volumetric rendering,” *J. Biomed. Opt.*, vol. 18, no. 2, p. 26002, Feb. 2013.
- [52] C. Wang *et al.*, “Multiplexed aberration measurement for deep tissue imaging *in vivo*,” *Nat. Methods*, vol. 11, no. 10, pp. 1037–1040, Oct. 2014.
- [53] C. Wang and N. Ji, “Pupil-segmentation-based adaptive optical correction of a high-numerical-aperture gradient refractive index lens for two-photon fluorescence

endoscopy,” *Opt. Lett.*, vol. 37, no. 11, pp. 2001–2003, Jun. 2012.

- [54] D. E. Milkie, E. Betzig, and N. Ji, “Pupil-segmentation-based adaptive optical microscopy with full-pupil illumination,” *Opt. Lett.*, vol. 36, no. 21, pp. 4206–4208, Nov. 2011.
- [55] D. J. Wahl, C. Huang, S. Bonora, Y. Jian, and M. V. Sarunic, “Pupil segmentation adaptive optics for invivo mouse retinal fluorescence imaging,” *Opt. Lett.*, vol. 42, no. 7, p. 1365, Apr. 2017.